



**HAL**  
open science

# Paleoenvironmental variations during the Late Cambrian: Implications from Zn isotopes, I/(Ca+Mg) ratios, and other elemental proxies

Luisa González Robacio, Karem Azmy, Bleuenn Guéguen, Francis Claret

## ► To cite this version:

Luisa González Robacio, Karem Azmy, Bleuenn Guéguen, Francis Claret. Paleoenvironmental variations during the Late Cambrian: Implications from Zn isotopes, I/(Ca+Mg) ratios, and other elemental proxies. *Marine and Petroleum Geology*, 2024, 165, pp.106817. 10.1016/j.marpetgeo.2024.106817 . hal-04582104

**HAL Id: hal-04582104**

**<https://brgm.hal.science/hal-04582104v1>**

Submitted on 11 Jul 2024

**HAL** is a multi-disciplinary open access archive for the deposit and dissemination of scientific research documents, whether they are published or not. The documents may come from teaching and research institutions in France or abroad, or from public or private research centers.

L'archive ouverte pluridisciplinaire **HAL**, est destinée au dépôt et à la diffusion de documents scientifiques de niveau recherche, publiés ou non, émanant des établissements d'enseignement et de recherche français ou étrangers, des laboratoires publics ou privés.

1 **Paleoenvironmental variations during the Late Cambrian: implications**  
2 **from Zn isotopes, I/(Ca+Mg) ratios, and other elemental proxies**

3 Luisa González Robacio <sup>1</sup>, Karem Azmy <sup>1\*</sup>, Bleuenn Guéguen <sup>2</sup>, Francis Claret <sup>3</sup>

4 <sup>1</sup> Department of Earth Sciences, Memorial University of Newfoundland, St. John's,  
5 Newfoundland A1B 3X5, Canada.

6 <sup>2</sup> Université de Rennes, CNRS, UAR 3343, Avenue du Général Leclerc, 35042 Rennes,  
7 France

8 <sup>3</sup> BRGM, 3 Avenue Claude Guillemin, 45060 Orléans Cedex 2, France

9 \*Corresponding author (email: [kazmy@mun.ca](mailto:kazmy@mun.ca))

10 **Abstract**

11 The Upper Cambrian at the Martin Point section (~110 m-thick) in western  
12 Newfoundland is a part of the Cow Head Group and partially spans the coeval Tuckers Cove  
13 and the Martin Point members of the Shallow Bay and Green Point formations, respectively.  
14 These units comprise alternating shale, minor conglomerate beds, and limestone rhythmites  
15 of a toe-of-slope apron. Earlier studies of the C-isotope profile, based on the lime mudstone  
16 interbeds, documented global negative  $\delta^{13}\text{C}_{\text{carb}}$  shifts (from old to young: NL1, NL2, HERB)  
17 correlated with the lowermost *Proconodontus posterocostatus*, *Proconodontus muelleri* and  
18 base of *Eoconodontus notchpeakensis* conodont zones, respectively (post-Steptoean Positive  
19 Carbon Isotope Excursion NL1 and NL2 and Hellnmaria-Red Tops Boundary-HERB).  
20 Samples were extracted from the most preserved spots of micritic to near-micritic grain size  
21 ( $\leq 4 \mu\text{m}$ – $10 \mu\text{m}$ ). Fabric retention confirms petrographic preservation and insignificant  
22 correlations ( $R^2 \leq 0.1$ ) of diagenetic proxies (e.g., Sr) with their environmental counterparts  
23 support the preservation of at least near-primary geochemical signatures. The  
24 paleoenvironmental proxies (TOC, Zn, P, Cu, Al/Ti, Mn, Fe, V, Mo) support dominant  
25 dysoxic conditions. The  $\delta^{66}\text{Zn}$  values (0.09–0.73 ‰ JMC Lyon) and I/(Ca+Mg) ratios  
26 (0.02–0.48  $\mu\text{mol/mol}$ ) vary consistently throughout the studied events. The minor decreases

27 in  $\delta^{66}\text{Zn}$  values seem to denote inhibition of bioproductivity in a dysoxic water column,  
28 consistent with warm and humid climate during general transgressive settings and shoaling of  
29 organic-rich water into the shallow environment. The low  $I/(\text{Ca}+\text{Mg})$  ratios ( $< 0.5 \mu\text{mol/mol}$ )  
30 reinforce this interpretation, suggesting general dysoxic settings throughout the entire section.

31 **Keywords:** Upper Cambrian paleoenvironment,  $I/(\text{Ca}+\text{Mg})$  ratios, Zn-isotopes, eastern  
32 Laurentia, Martin Point (western Newfoundland, Canada).

### 33 1. Introduction

34 Geochemistry of carbonates has been proven very reliable tool in understanding the  
35 paleoenvironmental and paleoclimatic aspects of the Earth's history. It allows the evaluation  
36 of diagenetic influence and inferring parameters such as salinity, temperature, density, pH,  
37 fluvial influx, weathering rate, paleoredox, and bioproductivity (e.g., Algeo and Maynard;  
38 2004; Kasemann et al., 2009; Veizer et al., 1999; Śliwiński et al., 2010; Nakada et al., 2013;  
39 Rostovtseva and Kuleshov, 2016; D'Arcy et al., 2017; Scholz et al., 2017; Niu et al., 2018).

40 Zinc ( $^{64}\text{Zn}$ ,  $^{66}\text{Zn}$ ,  $^{67}\text{Zn}$ ,  $^{68}\text{Zn}$ , and  $^{70}\text{Zn}$  with average natural abundances of 48.6, 27.9,  
41 4.1, 18.8, and 0.6%, respectively) is a bio-limiting micronutrient that follows a nutrient-type  
42 profile in the ocean, where surface water is relatively depleted compared with deep water due  
43 to biological pumping and re-precipitation and recycling of organic matter in deeper water  
44 and dissolution of sinking particles (Bruland, 1980; Morel et al., 1994). Estimates of the Zn  
45 residence time in modern oceans range between 1,000 and 11,000 years (Hayes et al., 2018).  
46 Zinc occurs in seawater in the form of hydroxide and carbonate complexes (Millero, 1996)  
47 and is incorporated in carbonate minerals in trace amounts, both as tetrahedral complexes on  
48 the calcite surface and substituting  $\text{Ca}^{2+}$  in the crystal lattice (Reeder et al., 1999). It appears  
49 to be an ideal substitution for  $\text{Ca}^{2+}$  since it is strongly enriched in the solid during co-

50 precipitation with calcite (Reeder et al., 1999), thus carbonates may potentially be good  
51 candidates for tracking past seawater Zn-isotope composition.

52 While deep ocean  $\delta^{66}\text{Zn}$  value is relatively homogeneous worldwide ( $\sim 0.5\text{‰}$ ; e.g.,  
53 Bermin et al., 2006; Boyle et al., 2012; Conway and John, 2014; Conway and John, 2015;  
54 Conway et al., 2013; Horner et al., 2021; John and Conway, 2014; Liao et al., 2020; Takano  
55 et al., 2017; Vance et al., 2019; Vance et al. 2017), surface water  $\delta^{66}\text{Zn}$  values are variable  
56 from  $-1.1\text{‰}$  to  $+1.2\text{‰}$  (Conway et al., 2013; Conway and John 2014; Zhao et al 2014;  
57 Samanta et al., 2017; John et al., 2018; Wang et al., 2018; Vance et al., 2019; Liao et al.,  
58 2020; Sieber et al., 2020; Horner et al., 2021). This variability is largely due to the  
59 preferential uptake of isotopically light  $^{64}\text{Zn}$  by microorganisms (Andersen et al., 2011;  
60 Conway and John, 2014; John and Conway, 2014; Samanta et al., 2017; Köbberich and  
61 Vance, 2019), although this pattern is not systematically observed (e.g., in the Southern  
62 Ocean, Zhao et al., 2014). The Zn-isotope ratios in surface waters are probably strongly  
63 influenced by scavenging and adsorption of Zn onto organic matter (John and Conway, 2014;  
64 John et al., 2018; Weber et al., 2018). However, aerosol and anthropogenic sources might  
65 also contribute to the Zn biogeochemical cycling (Conway and John, 2014; Lemaitre et al.,  
66 2020; Liao et al., 2020) in addition to intracellular regeneration of isotopically light  $^{64}\text{Zn}$   
67 (e.g., in the North Pacific Ocean, Vance et al., 2019).

68 Since Zn isotopes are fractionated during biological activity with preferential uptake  
69 of isotopically light  $^{64}\text{Zn}$  by organisms in seawater (Andersen et al., 2011; Conway and John,  
70 2014; John and Conway, 2014; Samanta et al., 2017; Köbberich and Vance, 2019), the Zn-  
71 isotope composition of carbonate has been used as a proxy for investigating fluctuations in  
72 primary productivity through time (Pichat et al., 2003; Kunzmann et al., 2013; John et al.,  
73 2017; Liu et al., 2018; Lv et al., 2018; Wang et al., 2018; Yan et al. 2019; Chen et al., 2021).  
74 However, the use of bulk carbonate  $\delta^{66}\text{Zn}$  composition as a proxy for seawater composition is

75 not straightforward. Müsing et al. (2022) suggest that  $\delta^{66}\text{Zn}$  values in bulk carbonates are  
76 more likely to record variations in the mechanisms of incorporating Zn. Besides, large  $\delta^{66}\text{Zn}$   
77 variations were shown in shallow water carbonates from the Bahamas where the  $\delta^{66}\text{Zn}$  values  
78 of carbonate muds were  $\sim 0.3\%$  higher than ambient seawater (Zhao et al., 2021). However,  
79 the  $\delta^{66}\text{Zn}$  values of carbonate ooids, peloids, skeletal and microbial aragonites, green algae,  
80 stromatolites, and precipitates associated with cyanobacterial filaments were similar to  
81 ambient seawater  $\delta^{66}\text{Zn}$  values (Zhao et al., 2021). Deep-sea corals are also promising for  
82 faithfully recording deep seawater  $\delta^{66}\text{Zn}$  values (Little et al., 2021) while shallow-water  
83 corals may be good tracers of surface seawater composition (Zhang et al., 2022). In addition,  
84 it is necessary to assess the effect of diagenesis to confirm that the signatures are primary or  
85 at least near-primary (Hohl et al., 2015).

86 Iodine is present in seawater as the thermodynamically stable dissolved forms of  
87 iodate ( $\text{IO}_3^-$ ) and iodide ( $\text{I}^-$ ) (Wong and Brewer, 1977). As iodine is highly redox-sensitive,  
88 its speciation change iodide/iodate has been proposed to be a redox proxy (Liss et al., 1973).  
89 It occurs mainly as iodate under well-oxygenated conditions (Truesdale and Bailey, 2000) but  
90 as the water column oxygen concentrations decrease, the iodate is reduced to iodide  
91 (Bowman et al., 2021), which dominates in anoxic basins and porewaters (Wong and Brewer,  
92 1977). Iodate is the sole anion incorporated into the carbonate structure (Lu et al., 2010; Feng  
93 and Redfern, 2018), as it partially substitutes  $\text{CaCO}_3^{2-}$ , while iodide cannot enter the  
94 structure, likely due to the large ionic radius of iodide relative to iodate (Zhou et al., 2015).  
95 Iodate accumulates in planktonic and benthic marine calcifiers and, ultimately, trace amounts  
96 compose carbonate rocks (Fuge and Johnson, 1986). The Iodine to calcium ratio (I/Ca) is  
97 independent of  $\text{I}^-$  in parent waters, but affected by the  $\text{IO}_3^-$  concentration in water in a linear  
98 relationship (Lu et al., 2010). Therefore, the ratio, expressed as  $\text{I}/(\text{Ca}+\text{Mg})$ , is a useful tracer

99 in carbonates for redox conditions in the geological past (e.g., Lu et al., 2010; Zhou et al.,  
100 2015).

101 The Cambrian was a period with an overall warm temperature and progressive sea-  
102 level rise but marked by brief episodes of abrupt changes (e.g., Babcock et al., 2015). These  
103 events seem to be recorded in the  $\delta^{13}\text{C}$  values of carbonates and, during the Furongian,  
104 distinctive global shifts have been documented including the post-SPICE (post-Steptoean  
105 Positive Carbon Isotope Excursion; Li et al., 2006; Azmy, 2019b) and the HERB  
106 (Hellnmaria-Red Tops Boundary; Miller et al., 2011; Li et al., 2017; Azmy, 2019b) events.  
107 The investigated section at Martin Point (western Newfoundland, Canada) spans the post-  
108 SPICE and HERB events.

109 The main objectives of the current study are:

- 110 • To evaluate the preservation of the Zn isotope and  $I/(\text{Ca}+\text{Mg})$  signatures retained in  
111 the Martin Point section carbonates.
- 112 • To investigate the variations of Zn isotopes and  $I/(\text{Ca}+\text{Mg})$  ratios in the late Cambrian  
113 ocean water to reconstruct the paleoenvironmental conditions during that time  
114 interval.
- 115 • To shed light on the variations in the paleoredox conditions reconstructed from other  
116 elemental proxies.

## 117 **2. Geological Setting**

118 Western Newfoundland is the northeast extension of the Appalachian mountain range  
119 in Canada (Fig. 1) that forms a part of the Humber Zone tectonostratigraphic terrane  
120 (Williams, 1978) and has the best-preserved successions of the early Paleozoic margin of  
121 Laurentia (North America). The successions overlie unconformably the Grenvillian basement  
122 and record parautochthonous sedimentary units from the Cambrian to Silurian and  
123 allochthonous units containing sedimentary, igneous, and metamorphic rocks (James and

124 Stevens, 1986; Quinn et al., 1999; Cooper et al., 2001). The transported rocks were  
125 structurally emplaced onto the Laurentian margin during the Taconian and Acadian orogenies  
126 (~ 440 Ma and ~ 416 Ma, respectively) and constitute the Humber Arm Allochthon in the  
127 south of western Newfoundland, of which the sedimentary rocks are called the Humber Arm  
128 Supergroup (Stevens, 1970).

129         During the Neoproterozoic rifting of Rodinia, seafloor spreading between Laurentia  
130 and west Gondwana resulted in the opening of the Iapetus Ocean (Cawood et al., 2001) and  
131 the establishment of the Laurentian margin (Waldron et al., 1998), which developed during  
132 the latest Precambrian to early Cambrian. A succession of variable thickness of terrestrial  
133 arkosic sandstones, conglomerates, graywackes, quartzites, and local thick volcanic units and  
134 mafic dykes deposited during rifting and continental breakup (Williams and Hiscott, 1987).  
135 On the other hand, the overlying assemblage shows a more homogeneous thickness and  
136 lateral continuity and represents a marine succession deposited during the thermal subsidence  
137 of the margin and development of a carbonate platform.

138         In western Newfoundland, the Bateau, Lighthouse Cove, and Bradore formations  
139 (Labrador Group) embody the synrift rocks, the transition from rift to passive margin lying  
140 within the Bradore Formation (Allen et al., 2010) or at its base (Cawood et al., 2001). The  
141 Forteau Formation from the same group represents the thermal subsidence of the margin and,  
142 thus, an extensive marine transgression (Williams and Hiscott, 1987) on a mainly siliciclastic  
143 shelf. During the Middle to Late Cambrian, the high-energy carbonate platform of the Port au  
144 Port Group developed, followed by the St. George Group's low-energy carbonate platform  
145 (Early Ordovician) and a carbonate bank belonging to the Table Head Group (Middle  
146 Ordovician), which determines the final phase of the passive-margin sequence (Stenzel et al.,  
147 1990).

148           The allochthonous sedimentary rocks of the Humber Arm Supergroup span the Early  
149 Cambrian to Middle Ordovician and are divided into two deep-water units: the Curling and  
150 the Cow Head Group (Fig. 1). They register the passive continental margin and foredeep  
151 environments, and a record of rifting, continental margin subsidence and continent-arc  
152 collision (Waldron and Palmer, 2000). The Cow Head Group was deposited along the  
153 continental southeast-dipping slope as debris shed from the platform into deeper water  
154 (Williams and Hiscott, 1987; Lacombe et al., 2019), forming an extensive sedimentary apron  
155 with a proximal-distal polarity from northwest to southeast, which translates into the Shallow  
156 Bay and the Green Point formations, respectively (James and Stevens, 1986).

157           The Humber Arm Allochthon rocks disposed of as a series of thrust slices (White and  
158 Waldron, 2018) accreted onto the Laurentian margin, as the Taconian orogenesis began in the  
159 Early Ordovician with westward thrust signaling the first effect of the closure of the Iapetus  
160 Ocean in western Newfoundland (Waldron et al., 1998). The Cow Head Group is  
161 stratigraphically overlain by flysch due to the development of a foreland basin (Quinn, 1992).  
162 Deformation generated by the Acadian orogenesis during the Devonian was imprinted, in a  
163 later stage, on the Taconian thrusts and melange belts (Cousineau and Tremblay, 1993; White  
164 and Waldron, 2018).

### 165           **3. Stratigraphy**

#### 166           **3.1. Lithostratigraphy**

167           The Cow Head Group lithostratigraphy (Fig. 2) was extensively described and  
168 discussed by James and Stevens (1986). The unit is dominated by rhythmites that were  
169 deposited at the foot of a continental slope, as a mixture of fine-grained hemipelagites and  
170 sediment gravity flows, which consist of alternations of shales, siltstones, and limestones.

171           The shales are laminated and vary from black to dark grey and green due to  
172 deposition under anoxic to dysoxic conditions, or appear red and bioturbated. The dolomitic

173 siltstones and silty dolomites are buff weathering and combine both detrital and diagenetic  
174 deposits. Interlaminations of shales and siltstone occur in association with turbidite deposits  
175 (Coniglio, 1985; Bouma, 1962; Stow and Shanmugam; 1980).

176 Carbonates occur as ribbons (alternations of interbeds of carbonates and argillaceous  
177 layers with similar thickness) or parted limestones (argillaceous layers significantly thinner)  
178 (James and Stevens, 1986). These rhythmites appear like planar, lumpy beds or nodules in  
179 shale and their textures include lime mudstones (Dunham, 1962), graded calcisiltite, and  
180 rippled calcarenite.

181 Quartzose calcarenites show coarse to very coarse grains with rounded and spherical  
182 shapes (typical eolian quartz), and ooids whereas algal bioclasts constitute mainly the  
183 allochems. These rocks can be massive because of grain flows, graded as in turbidite deposits  
184 or disposed as caps on top of conglomerates. Coniglio (1985) proposed that the turbidite  
185 deposits are a result of high-density turbidity currents.

186 The Cow Head Group (Figs. 1 and 2) comprises two coeval formations: the Shallow  
187 Bay Formation, of which the Tuckers Cove Member constitutes the lower part of the  
188 currently investigated section at Martin Point, and the overlying Green Point Formation, of  
189 which the Martin Point Member constitutes the upper part of that section. These two  
190 members formed when the deposition of the sediment apron changed to mainly quartz-rich  
191 calcarenites with shales and minor conglomerates (Tuckers Cove Member), grading distally  
192 into the Martin Point Member lithology, as the sand wedge was considerably widespread.

193 The proximal Shallow Bay Formation (100–300 m) is composed of a sequence of  
194 limestone conglomerate and calcarenite with interbedded limestone and shale in the upper  
195 part. The Tuckers Cove Member is the uppermost member of the Shallow Bay Formation and  
196 consists of interbedded quartzose calcarenite, graded stratified conglomerate to occasional

197 boulder conglomerate, minor parted to ribbon limestone separated by green calcareous shale,  
198 sandstone, buff-weathering, well-laminated or rippled dolomitic siltstones and thin black  
199 shale (James and Stevens, 1986).

200 The occurrence of the quartzose calcarenites decreases in the upper half of the  
201 Tuckers Cove Member, while the parted and ribbon limestone and conglomerates become  
202 more frequent in the investigated Martin point section, and conglomerates only represent a  
203 minor portion of the succession (James and Stevens, 1986). Kindle and Whittington (1958)  
204 suggested that the conglomerates are the result of slumping processes whereas Hubert et al.  
205 (1977) proposed that debris flow is the responsible mechanism.

206 On the other hand, the distal Green Point Formation (400–500 m) occurs as fine-  
207 grained facies and the strata are mostly green, red, and minor black shale with occasional  
208 conglomerate and ribbon-to-parted limestone. The Martin Point Member (100–150 m) is the  
209 basal unit and is composed of green and black shale with partings of thin buff-weathering  
210 siltstone and calcareous sandstone, layers of ribbon and parted limestone, and scarce thin  
211 conglomerate beds.

### 212 3.2. Biostratigraphy

213 The investigated interval comprises the uppermost Franconian to the Trempealeuan  
214 (Furongian, uppermost Cambrian). The conodont biozonation scheme (Fig. 2) of the Cow  
215 Head Group along the Cambrian-Ordovician boundary was widely described by Bagnoli et  
216 al. (1986), Barnes (1988), and James et al. (1989). Zhang and Barnes (2004) included in their  
217 study the Broom Point North section (lower proximal slope facies of the Tuckers Cove  
218 Member) and the Green Point section (distal slope facies of the Martin Point Member). The  
219 Tuckers Cove Member contains the *Eoconodontus notchpeakensis* zone in Broom Point  
220 North, while Martin Point Member has also the *Cordylodus proavus* and the *Cordylodus*  
221 *Caboti* zones, and part of the *Cordylodus Intermedius* zone in Green Point. This same

222 interval, where FAD of *C. Intermedius* occurs at the Green Point GSSP, is correlated with the  
223 top (James and Stevens, 1986) of the Martin Point Member at the Martin Point section  
224 (Stouge et al., 2017).

225 Thus, the investigated Martin Point section (Fig. 2) spans, from bottom to top, the  
226 upper part of the *Proconodontus posterocostatus*, the *Proconodontus muelleri*, the  
227 *Eoconodontus notchpeakensis* (e.g., Lawson Cove and Sneakover Pass sections in Utah,  
228 USA), the *C. proavus*, and the *C. Caboti* conodont zones on the global and North American  
229 conodont biozonation scheme (James and Stevens, 1986; Barnes, 1988; Miller et al., 2011; Li  
230 et al., 2017). The base of the *Eoconodontus notchpeakensis* Zone is marked by the global  
231 Uppermost Cambrian HERB  $\delta^{13}\text{C}$  excursion (Li et al., 2017) that has been also documented  
232 in the Green Point (Cambrian-Ordovician GSSP; Miller et al., 2011) and Martin Point (Azmy  
233 2019a) sections. However, the *Proconodontus posterocostatus* and *Proconodontus muelleri*  
234 zones have not been documented yet in the Martin Point section. The Cambrian Stage 10  
235 spans almost from the *P. posterocostatus* to *C. caboti* (at the Cambrian-Ordovician boundary)  
236 conodont zones (Fig. 2) and its base is marked by a negative  $\delta^{13}\text{C}$  excursion (N1) on the C-  
237 isotope profile of the Wa'ergang section in China (Li et al., 2017). A correlated  $\delta^{13}\text{C}$   
238 excursion (NL1) has been also documented by the Martin Point C-isotope profile (Figs. 1b  
239 and 2; Azmy, 2019b).

240 The investigated carbonates span the Upper Cambrian and their C-isotope stratigraphy  
241 (Fig. 2) records two post-SPICE (Steptoean Positive Isotope Excursion) negative excursions  
242 (NL1 and NL2; Azmy, 2019b) and the overlying HERB negative excursion (Azmy, 2019a;  
243 Wang and Azmy, 2020). The paleoenvironmental proxies of the HERB event (recorded by  
244 the upper Martin Point section) have been studied by Wang and Azmy (2020) and the current  
245 study investigates the variations in the  $\delta^{66}\text{Zn}$  and I/Ca+Mg) across both of the post-SPICE

246 and HERB events including the paleoenvironmental proxies of the post-SPICE carbonates  
247 (recorded by the lower Martin Point section).

248 The sequence of conodont zones can be correlated with trilobite zones *Saukia* (from  
249 bottom to top, subzones *Rasettia magna*, *Saukiella junia*, *Saukiella serotina*, *Corbina*  
250 *apopsis*) and *Missisquoia* (subzones *Missisquoia depressa*) from the Upper Cambrian and  
251 lowest Ordovician found in the Wichita Mountains area (Barnes, 1988; Stitt, 1977; Fig. 2).

## 252 **4. Methodology**

### 253 **4.1. Sampling and elemental analysis**

254 A hundred and thirteen lime mudstone samples (Azmy 2019a,b; Appendix 1; Fig. 2)  
255 were collected from the most micritic lime mudstone interbeds at the Martin Point section  
256 (49° 40' 51" N, 57° 57' 36" W; Fig. 1; James and Stevens, 1986; Cooper et al., 2001), western  
257 Newfoundland, at high resolution with intervals as narrow as 30 cm (Fig. 2). Representative  
258 sample selection was guided by results from an earlier C-isotope stratigraphic study on the  
259 same succession (Azmy, 2019a,b). Thin sections of the micritic carbonates were stained with  
260 Alizarin Red-S and potassium ferricyanide solutions (Dickson, 1966) before petrographic  
261 examination using a polarizing microscope to locate the most micritic spots.  
262 Cathodoluminescence (CL) examination was performed with a Technosyn 8200 MKII cold  
263 cathode instrument operated at 8 kV accelerating voltage and 0.7 mA current. Minor organic  
264 matter (sporadically along stylolites and solution seams) and rare microfractures (filled with  
265 carbonate cement) were avoided during microsampling.

266 The mirror-image slab of each thin section was polished, cleaned with deionized  
267 water in an ultrasonic bath, and dried overnight at 40°C before sampling. Samples (~200 mg  
268 each) were extracted from the most micritic material of the cleaned slab.

269 For trace elements analyses, 47 powder samples (each ~100–200 mg) were weighted,  
270 digested in HCl-HNO<sub>3</sub> (to digest carbonate only), centrifuged to remove any trace insoluble  
271 material, and evaporated to dryness. Residues were then dissolved in 5 mL 6N HCl and  
272 centrifuged to remove undissolved organic matter and kept as archive solutions. An aliquot of  
273 the archive solution was collected and diluted in 2.5% HNO<sub>3</sub> for analysis on an HR-ICP-MS  
274 (Element XR, Thermofisher Scientific) at Pôle de Spectrométrie Océan (PSO, IUEM, Brest,  
275 France). Indium was used as the internal standard for signal drift correction and  
276 concentrations were calibrated using external calibration standards. The relative uncertainties  
277 of the measurements are better than 5% using the BHVO2 standard.

278 The elemental paleoenvironmental proxies were normalized to Ca following the  
279 equation (e.g., Hardisty et al., 2017):

280  $X_{CaN} = (X/X_{\text{atomic weight}})_{\text{Sample}} / (Ca_{\text{sample}}/40.078)$  where X is the proxy element. Due to  
281 the low values of ratios, they were expressed in micromole/mole ( $\mu\text{mol/mol}$ ) and  
282 millimole/mole ( $\text{mmol/mol}$ ).

#### 283 **4.2. Zn-isotope Analysis**

284 Zinc isotopes were separated from the matrix with ion-exchange chromatography  
285 columns following a procedure adapted from Maréchal et al. (1999). Briefly, 2 mL of  
286 macroporous AG MP-1 resin (100–200 mesh Biorad) was loaded on polypropylene columns.  
287 The resin was cleaned with 10 mL deionized water, 8 mL HNO<sub>3</sub>, and again with 10 mL  
288 deionized water. Before sample loading, the resin was conditioned with 4 mL 6N HCl. An  
289 aliquot of the sample archive solution prepared for trace elements analyses was loaded on the  
290 column in 6N HCl. The matrix was eluted in 2.5 mL 6N HCl, 10 mL 2N HCl, and 4 mL  
291 0.24N HCl, and Zn was collected in 18 mL 0.012N HCl. The solution was evaporated to  
292 dryness on a hot plate at 90°C and the residue was dissolved in 2.5% HNO<sub>3</sub> for isotopic  
293 analyses.

294 Zinc isotopes were measured by MC-ICP-MS (Neptune Thermofisher Scientific) at  
295 Pôle de Spectrométrie Océan (PSO, Ifremer, Brest, France) in low-resolution mode using the  
296 Cu-doping method (Cu NIST SRM 3114) to correct for instrumental mass bias (Maréchal et  
297 al., 1999). A standard-sample-bracketing method was applied by measuring the isotopic  
298 standard Zn NIST SRM 683 doped with Cu NIST SRM 3114 before and after each sample.  
299 Zinc isotopes are reported in the conventional delta notation:

$$300 \quad \delta^{66}\text{Zn} (\text{‰}) = [({}^{66}\text{Zn}/{}^{64}\text{Zn})_{\text{sample}}/({}^{66}\text{Zn}/{}^{64}\text{Zn})_{\text{SRM683}} - 1] \times 1000$$

301 However, for consistency with values reported in the literature, the Zn isotope  
302 composition is reported relative to the JMC-Lyon isotopic standard (Archer et al., 2017). The  
303 precision of analyses is reported as  $2\sigma$  calculated based on replicate measurements of the  
304 standard Zn NIST SRM 683. The precision was better than 0.06 ‰ and was determined using  
305 the USGS and BHVO-2 standards for which three aliquots were processed on three different  
306 columns following the same procedure applied to samples. The total Zn in blank was <5 ng.

### 307 **4.3. I/(Ca+Mg) Analysis**

308 The I/(Ca+Mg) measurements (Appendix 1) were run following the protocol  
309 suggested by Hardisty et al. (2017). Thirty powdered samples (~ 3–5 mg each) were  
310 sonicated in 1 mL of deionized water, centrifuged, and decanted. Samples were digested in  
311 3% HNO<sub>3</sub>, sonicated for ~10 minutes, and centrifuged. The supernatant was diluted with  
312 nitric acid and 0.25 % tetramethyleammonium hydroxide (TMAH) before running on an  
313 Agilent 8900 triple quad inductively coupled plasma mass spectrometer (ICPMS). Blanks,  
314 international (VWR AVS titrino IC 1000 mg/L), and internal standards were also prepared  
315 and treated similarly. Analytical uncertainties (monitored by Alfa Aesar's 0.1 N potassium  
316 iodate) were better than 5%.

317

## 318 5. Results

319 Petrographic examination, including cathodoluminescence (CL), shows that the  
320 investigated carbonates are mainly non-ferroan lime mudstones, dominated by micritic ( $\leq 4$   
321  $\mu\text{m}$ ) to near-micritic ( $\sim 10 \mu\text{m}$ ) grain size and they appear non-luminescent under the CL (Fig.  
322 3).

323 The chemical attributes are tabulated in Appendix 1 and Table 1 summarizes their  
324 statistics. The mean values of the investigated paleoenvironmental proxies of the post-SPICE  
325 and HERB events are generally comparable. The mean  $\delta^{66}\text{Zn}$  values in both intervals are  
326 almost identical ( $\sim 0.3 \pm 0.1 \text{‰}$  JMC-Lyon; Table 1) and similar to average continental crust  
327 ( $\delta^{66}\text{Zn} = 0.31 \pm 0.11\text{‰}$ ; Little et al., 2014). Similarly, those of  $\text{I}/(\text{Ca}+\text{Mg})$  are very  
328 comparable (0.1 and 0.2  $\mu\text{mol}/\text{mol}$ , respectively; Table 1) and less than the lower boundary  
329 value established for oxic conditions (2.5  $\mu\text{mol}/\text{mol}$ , Lu et al., 2016). The carbonates of the  
330 upper (spanning the post-SPICE NL1 and NL2 events) and lower (spanning the HERB event)  
331 Martin Point section have comparable elemental compositions with ranges that generally  
332 overlap except for some higher Al values in the lower section (Fig. 4; Table 1)

333 The Sr values in the post-SPICE and HERB carbonates ( $290 \pm 184 \text{ ppm}$  and  $356 \pm$   
334  $226 \text{ ppm}$ , respectively; Table 1; Fig. 4) are also comparable. They exhibit mainly  
335 insignificant correlations ( $R^2 < 0.02\text{--}0.13$ ) with their Zn, P, Ni, Cu, Fe, Th/U,  $\Sigma\text{REE}$ , Al, Mn,  
336 Fe,  $\delta^{66}\text{Zn}$ , and  $\text{I}/(\text{Ca}+\text{Mg})$  counterparts (Fig. 4) or an opposite trend to that expected from  
337 diagenetic alterations (Fig. 4b). The profiles, reconstructed from the Ca-normalized molar  
338 ratios, exhibit minor variations correlated with NL1 but more pronounced shifts with NL2 of  
339 the post-SPICE interval (Fig. 5). On the other hand, most of these profiles show noticeable  
340 variations correlated with the HERB event (Fig. 5).

341

## 342 **6. Discussion**

### 343 **6.1 Evaluation of the diagenetic impact**

#### 344 ***6.1.1 Petrographic Preservation***

345 The petrographic preservation of the Martin Point carbonates is summarized here  
346 since it has been already discussed in detail by Azmy (2019a,b) and Wang and Azmy (2020).  
347 Petrographic examination of the studied carbonates indicates that they are mainly fabric-  
348 retentive lime mudstones with minimum recrystallization. They are dominated by micritic  
349 (<4  $\mu\text{m}$ ) to near-micritic (10  $\mu\text{m}$ ) grain size (Fig. 3a,c) and exhibit dull to non-CL (Fig. 3b,d),  
350 which suggest low water/rock interaction ratios and a high degree of petrographic  
351 preservation. Cathodoluminescence (CL) in carbonates is controlled by trace element  
352 contents (Machel and Burton, 1991; Machel, 2000), of which  $\text{Mn}^{2+}$  and  $\text{Fe}^{2+}$  are the most  
353 important cations substituting  $\text{Ca}^{2+}$  in the crystal lattice (Leverenz, 1950) and acting as  
354 activator and quencher, respectively.

355 However, the CL technique is only complementary, for it has been demonstrated that  
356 cation exchange can occur without significant visible change in the crystal size, and fracture-  
357 filling cement of deep-burial settings may have high Fe and exhibit also dull CL (Rush and  
358 Chafetz, 1990). Therefore, petrographic examination alone cannot confirm sample  
359 preservation but has to be combined with other tools. Yet, if redistribution of mass takes  
360 place within length scales over which the system is fundamentally closed and this length  
361 scale is smaller than sampling, a fairly faithful signal can be recovered (Fantle et al., 2020).

#### 362 ***6.1.2 Geochemical preservation***

363 Progressive burial of carbonates is associated with an increase in temperature and  
364 the reaction of sediments with the diagenetic fluids results in the depletion of some elements  
365 such as Sr but enrichment of others such as Mn, Fe, Al, and  $\sum\text{REE}$  (Veizer, 1983; Azmy et  
366 al., 2011; Wang and Azmy, 2020). However, diagenesis might not significantly influence

367 other geochemical proxies (e.g., Ni, P, Zn, Th, U,  $\delta^{66}\text{Zn}$ , and  $\text{I}/(\text{Ca}+\text{Mg})$ ) leaving their  
368 signatures with at least a near-primary nature, which therefore makes them reliable  
369 environmental proxies (Veizer, 1983; Śliwiński et al., 2010; Pattan et al., 2013; Acharya et  
370 al., 2015; Yan et al., 2019; Wörndle et al., 2019).

371 The Sr values, a reliable independent proxy of carbonate diagenesis (Veizer, 1983),  
372 show insignificant ( $R^2 \leq 0.1$ ) correlations (Fig. 4) with their  $\delta^{13}\text{C}$ , TOC, P, Ni, Zn,  $\delta^{66}\text{Zn}$ , Al,  
373  $\sum\text{REE}$ , Mn, Fe, V, U, Th/U, and  $\text{I}/(\text{Ca}+\text{Mg})$  values, which is also evident from the Sr profile  
374 (Fig. 5). This is consistent with the petrographic preservation (Fig. 3; Azmy 2019a,b; Wang  
375 and Azmy, 2020) and also supports the preservation of at least near-primary geochemical  
376 signatures. The deposition of the investigated Martin Point lime mudstones in dysoxic  
377 settings, as suggested from the sedimentological evidence (James and Stevens, 1986;  
378 Landing, 2012; Azmy, 2019a and b; Wang and Azmy, 2020), likely contributed to the  
379 relatively higher Mn and Fe contents (Fig. 4; Table 1) than their modern counterparts  
380 (Morrison and Brand, 1986).

381 The Mg/Ca ratios have insignificant correlations with their  $\delta^{66}\text{Zn}$  and  $\text{I}/(\text{Ca}+\text{Mg})$   
382 counterparts ( $R^2 = 0.0009$  and  $0.02$ , respectively; Appendix 1). Iodine is incorporated into the  
383 calcite crystal as  $[\text{IO}_3]^-$  and not  $[\text{I}]^-$  (Lu et al., 2010) and minor alteration or dolomitization of  
384 carbonates, particularly when early and lacks a significant increase in crystal size (aggrading  
385 neomorphism) or loss of sedimentary fabric, is therefore unlikely to influence their iodine  
386 contents. A recent study by Lu et al. (2021) documented no difference in the  $\text{I}/(\text{Ca}+\text{Mg})$   
387 ratios of non-crystallized and recrystallized samples. Although a study by Hashim et al.  
388 (2022) suggested that dolomitization might influence the  $\text{I}/(\text{Ca}+\text{Mg})$  ratios, their results were  
389 based on experimental high-temperature dolomitization, which makes the issue invalid for the  
390 currently investigated carbonates since they are dominantly lime mudstones and their

391 preserved micritic to near-micritic grain size and also sedimentary fabrics argue for early-  
392 stage diagenesis at near-surface temperature.

393 In addition, the insignificant correlation of the  $I/(Ca+Mg)$  ratios with the TOC values  
394 ( $R^2= 0.06$ ) argues against contributions from iodine associated with organic matter (Togo et  
395 al., 2016; He et al., 2020). Similarly, the insignificant correlation of the  $I/(Ca+Mg)$  with their  
396  $[Al]$  values ( $R^2= 0.19$ ; Appendix 1) and  $\delta^{66}Zn$  ratios with  $[Al]$  and  $\sum REE$  ( $R^2=0.006$  and  
397  $0.001$ , respectively; Appendix 1) eliminates iodine or Zn contaminants from clay minerals  
398 (siliciclastic inclusions).

399 In summary, the petrographic and geochemical criteria of the investigated lime  
400 mudstones support the retention of at least near-primary geochemical signatures that reflect  
401 variations in the paleoenvironment during deposition.

## 402 **6.2. Paleoenvironmental conditions**

403 Unlike siliciclastics, carbonates precipitate directly from seawater, thus recording the  
404 geochemical signatures in equilibrium with the ambient seawater. The relative fluctuations of  
405 sea level led to variations in seawater chemistry and that of marine carbonates, whose  
406 geochemical signatures are sensitive recorders of changes in environmental conditions (e.g.,  
407 Meyer et al., 2012). In the current study, trace element contents and Zn isotope compositions,  
408 as well as  $I/(Ca+Mg)$  ratios, are correlated with the  $\delta^{13}C_{carb}$  (Azmy, 2019a,b),  $\delta^{13}C_{org}$ , and  
409 TOC variations associated with the Late Cambrian NL1, NL2, and HERB events in western  
410 Newfoundland to reconstruct the paleoenvironmental conditions that dominated in eastern  
411 Laurentia during that time interval.

### 412 **6.2.1 Trace element proxies**

#### 413 **6.2.1.1. Primary productivity proxies**

414

415 The TOC profile, which has been utilized as the most direct proxy for primary  
416 productivity (Schoepfer et al., 2015), does not suggest high organic activity throughout the

417 entirely investigated section (Fig. 5). The mean TOC values are overall low for the post-  
418 SPICE and HERB samples ( $0.70 \pm 0.66$  % and  $1.02 \pm 0.62$  %, respectively; Table 1). In  
419 comparison, TOC data from carbonate rocks deposited during the late Devonian Frasnian-  
420 Famennian biotic crisis (Wang et al., 2018; Chen et al., 2005) show a mean value of 0.13 %.  
421 Carbonates from Late Quaternary minor productivity settings recorded TOC values  $< 0.4$  %  
422 (Rühlemann et al. (1996) but high productivity TOC values from Ediacaran dolostones range  
423 from 0.01 to 4.84 % (Gao et al., 2020). Therefore, the relatively low TOC of the Martin Point  
424 carbonates might reflect restricted bioproductivity.

425 For the HERB event, Miller et al. (2011) identified the *Eoconodontus notchpeakensis*  
426 zone as part of a lowstand system tract (LST) during sea transgression. Shoaling of anoxic  
427 organic-rich water during sea-level rise probably led to the emplacement of organic matter,  
428 enriched with elements such as P, Ni, and Cu, into shallow-water settings and oxidation of  
429 organic matter lowered oxygen levels to create dysoxic conditions (Canfield, 1993, 1994;  
430 Böning et al., 2009; Gill et al., 2011; Landing, 2012, 2013; Gao et al., 2016; Landing and  
431 Webster, 2018; Li et al., 2020).

432 Miller et al. (2003, 2011) identified full LST to highstand system tract (HST) cycles  
433 within each of the *Proconodontus posterocostatus* and the *Proconodontus muelleri* zones that  
434 span the recognized NL1 and NL2 events, respectively, which their geochemical signatures  
435 are comparable to those of the HERB event (Fig. 5). Therefore, a similar transgression with  
436 minor fluctuations likely took place during each of the NL1 and NL2 events as well.

#### 437 **6.2.1.2. Paleoredox proxies**

438 The profiles of Mn and Fe may reflect variations in redox conditions (Fig. 5), since  
439 they represent the fraction of the elements that are not derived from terrigenous influxes  
440 (Acharya et al., 2015), thus allowing the evaluation of their enrichment relative to average  
441 crustal abundance (Tribovillard et al., 2012). Relatively abundant concentrations of Mn and

442 Fe in the water column would indicate more reducing conditions, as they become more  
443 soluble with less oxygenation (Middelburg et al., 1988). The lack of significant metal  
444 enrichment has been interpreted as sediments deposited within substantial oxygenated bottom  
445 water (Acharya et al., 2015).

446 The normalization of Mn and Fe to Al is often used to evaluate the enrichment of Mn  
447 and Fe in carbonates in comparison to the detrital background, i.e., this is the authigenic  
448 carbonate content in Mn and Fe (Clarkson et al., 2014). The Mn/Al and Fe/Al ratios of  
449 Martin Point carbonates (0.04–0.93 and 0.8–11.3, respectively; Appendix 1) are enriched  
450 relative to the upper continental crust values (0.0075 and 0.44, respectively; McLennan,  
451 2001), which supports the suggested dysoxic conditions.

452 Enrichment of V is bound to organic matter (Breit and Wanty, 1991; Hetzel et al.,  
453 2009) and has been associated with deep-water sediments under anoxic environments  
454 (Brumsack and Gieskes, 1983; Emerson and Husted, 1991; Acharya et al., 2015).  
455 Molybdenum commonly shows strong co-variation with V and is generally enriched in  
456 anoxic sediments as well (e.g., Anbar et al., 2007). It is removed from the solution to the  
457 sediments by adsorption to organic matter or by Fe-Mn oxy-hydroxides (Algeo and Maynard,  
458 2004). Vanadium concentrations in Martin Point carbonates range from 1.7 ppm to 39.4 ppm  
459 (Table 1). Dolenc et al. (2001) reported V concentrations (2–48 ppm) lower than 60 ppm for  
460 LST carbonates spanning the Permian-Triassic boundary. The Mo contents in the Martin  
461 Point carbonates spanning the post-SPICE and HERB intervals (0.04–11.7 ppm; Table 1) are  
462 also comparable to those of the lower-end member values of the Permo-Triassic boundary  
463 (Dolenc et al., 2001)). Additionally, the positive shifts during the NL2 and at the base and  
464 top of the HERB event in the Martin Point section (Fig. 5) show high enrichment in Mo in  
465 comparison with typical concentrations for marine carbonates (<1 ppm in Carboniferous  
466 carbonates; Voegelin et al., 2009), and continental crust values (1.5 ppm; McLennan, 2001).

467 Manganese, Fe, V, and Mo increased above average concentrations for carbonates likely due  
468 to the shoaling of deep anoxic waters associated with the transgressions during the NL1,  
469 NL2, and HERB events.

470 Thorium ( $\text{Th}^{4+}$ ) is mainly produced from the weathering of clays and is unaffected by  
471 redox changes in the water column. In contrast, U occurs in oxic water as  $[\text{U}^{6+}]$  (soluble  
472 uranyl carbonate) but in anoxic water as  $[\text{U}^{4+}]$  (insoluble uranous fluoride), which is trapped  
473 in marine carbonates (Wignall and Twitchett, 1996). Wignall and Twitchett (1996)  
474 established a threshold by which  $\text{Th}/\text{U} < 2$  indicates anoxic environments of deposition and  
475  $>2$  for oxic conditions. The high Th/U values at the NL1, NL2, and HERB events (Fig. 5)  
476 seem to be contrary to the dominant dysoxic conditions expected during transgression and the  
477 suggested shoaling scenario. Therefore, the increase in the Th/U values can be attributed to  
478 either high Th concentrations or low U concentrations. On the other hand, some previous  
479 studies on carbonates from different time intervals during the Earth's history documented  
480 inconsistent variations exhibited by the Th/U redox proxy profiles (e.g., Cheng et al., 2017;  
481 Jin et al., 2018; Algeo and Li, 2020; Liao et al., 2020; Zhao et al., 2022, Zhang et al., 2023),  
482 and the ratio has to be therefore taken with caution.

483 Low U contents have been found to be associated with slow bottom water renewal  
484 due to partial restriction of local basins (Algeo and Tribovillard, 2009; Li et al., 2022), which  
485 is compatible with the presence of micro-continents separated from the Laurentian margin by  
486 the Taconic Seaway during the Furongian (Li et al., 2022; White and Waldron, 2022).

487 Particularly during the HERB event, there was a possibility of enhanced Th addition  
488 by terrigenous inputs, as the positive shift in the Th/U behaves fairly parallel to its Al/Ti  
489 counterpart (Fig. 5). During a generally warm and humid climate that favored transgression,  
490 active chemical weathering and runoff (increase in Al/Ti) might have provided clays to the  
491 ocean. Continental crust-derived sediments have an average concentration of 10.7 ppm for Th

492 and 2.9 ppm for U (Taylor and McLennan, 1980; Taylor and McLennan, 1985), meaning that  
493 their expected Th/U ratio would be  $\sim 4$ . As the higher positive peaks in the investigated  
494 section approach these values (Fig. 5), enhanced chemical weathering of crustal rocks might  
495 have contributed to the high Th/U, which is still coherent with the suggested transgression  
496 scenario.

497 It has been shown that, in reducing systems with considerable depths, Th tends to be  
498 absorbed by some algae (e.g., red algae of deep settings), whereas U is less likely to bind  
499 with carbonate ions, resulting in higher Th/U values (Shao et al., 2017, Bengston et al.,  
500 2017). Since the investigated carbonates were transported down to the lower slope  
501 environment, this scenario might have also contributed to the Th/U positive shifts.

### 502 **6.2.2. Zn isotope composition**

503 The  $\delta^{66}\text{Zn}$  values of the Martin Point carbonates range from 0.09 to 0.73‰ (Table 1;  
504 Fig. 5). Although the high end-member  $\delta^{66}\text{Zn}$  value (0.73‰) of sample B32 is associated  
505 with the lowest Sr and highest Mg contents (Fig. 2; Appendix 1; Table 1), its other  
506 geochemical proxy signatures fall within the same range of the rest of lime mudstone (calcite)  
507 samples and no correlation has been found between the  $\delta^{66}\text{Zn}$  and Ca/Mg values ( $R^2 =$   
508 0.0009; Appendix 1). This is consistent with earlier studies, which suggested that dolomites  
509 may still retain at least their near-primary  $\delta^{66}\text{Zn}$  signatures (e.g., Kunzmann et al., 2013; Yan  
510 et al 2019). The  $\delta^{66}\text{Zn}$  profile shows a general long-term slight increase until the end of the  
511 HERB event, which is followed by a decrease. It exhibits also localized minor increments  
512 ( $\sim 0.1$  to  $0.3\%$ ) at the base of NL1, NL2, and HERB events (Fig. 5). In addition, the profile  
513 shows negative shifts, with variable values, during the NL1 and NL2 events but a small  
514 positive shift ( $\sim 0.2\%$ ) during the HERB event (Fig. 5). Most of these variations (e.g.,  
515  $\delta^{66}\text{Zn}_{\text{Martin Point carbonates}} = 0.33 \pm 0.12\%$ ) are slightly higher than the standard deviation value  
516 associated with the mean  $\delta^{66}\text{Zn}$  value of the modern seawater of  $\sim 0.45 \pm 0.10\%$  (e.g., Horner

517 et al., 2021), and therefore reflect no dramatic paleoenvironmental changes (e.g.,  $\delta^{66}\text{Zn}_{\text{Martin}}$   
518  $\text{Point carbonates} = 0.33 \pm 0.12\text{‰}$ ) although the minor decrease in the  $\delta^{66}\text{Zn}$  values correlated with  
519 NL1 and NL2 is still consistent with a decrease in primary productivity during the suggested  
520 dysoxic conditions (Fig. 5). On the other hand, the slight increase in the  $\delta^{66}\text{Zn}$  values during  
521 the HERB event could be due to (i) an increase in primary productivity favoring the uptake of  
522 light  $^{64}\text{Zn}$  by microorganisms, (ii) sequestration of light  $^{64}\text{Zn}$  by organic-rich sediments, or  
523 (iii) increase in continental weathering particularly phosphates (Pons et al., 2013). The HERB  
524 event is correlated with a negative shift of  $\sim 2\%$  on the TOC profile and a positive shift on  
525 the Zn profile, which argues against an increase in primary productivity. However, the same  
526 event is correlated with a slight increase in P (Fig. 5;  $\sim 100$  ppm, Appendix 1) that followed a  
527 decrease at the base of the event, this is in addition to the general dysoxic conditions that  
528 might have enhanced the effect. This is consistent with the trace elements data that suggest  
529 prevailing dysoxic conditions during the HERB, NL1, and NL2 events due to sea-level rise  
530 and poor oxygenation of Laurentian continental margins.

### 531 **6.2.3. I/(Ca+Mg) ratio**

532 In modern oceans, the iodine concentration is fairly uniform ( $0.45 \mu\text{mol/l}$ ; Elderfield  
533 and Truesdale, 1980) and principally controlled by the burial of organic carbon in marine  
534 sediments (Muramatsu and Wedepohl, 1998). The iodine cycle through seawater and  
535 sediments seems to be biologically and photochemically mediated (Spokes and Liss, 1996;  
536 Wong et al., 2018). Its budget in the ocean is not dramatically affected by riverine inputs,  
537 carbonate precipitation/dissolution, or hydrothermal fluxes (Lu et al., 2010).

538 On the other hand, iodine primary signatures are influenced by local redox conditions  
539 more than large-scale changes (Zhou et al., 2015) where iodine occurs in solution as  
540 dissolved iodide ( $\text{I}^-$ ) in more reducing settings, or as iodate ( $\text{IO}_3^-$ ) in oxygenated conditions  
541 since these are its most thermodynamically stable forms (Wong and Brewer, 1977). Although

542 both anions are monovalent, they have shown different behaviors in sorption processes (e.g.,  
543 Hu et al., 2005). Carbonate minerals only incorporate the oxidized species during  
544 precipitation, since  $\text{IO}_3^-$  appears to be an appropriate substitution for  $\text{CO}_3^{2-}$  in the crystal  
545 lattice (Podder et al., 2017). Therefore, their  $\text{I}/(\text{Ca}+\text{Mg})$  contents seem to be proportional to  
546 the iodate concentrations of the solution (Lu et al., 2010), and thus carbonates in the vicinity  
547 of waters depleted in oxygen record lower ratios (e.g., Hardisty et al., 2014; Hardisty et al.,  
548 2017; Lu et al., 2017). This, in addition to the iodine residence time in seawater ( $\sim 300,000$   
549 years; Broecker and Peng, 1982), which is much longer than that of mixing ocean water,  
550 allows the  $\text{I}/(\text{Ca}+\text{Mg})$  ratio to behave as an indicator of redox variations in the ambient water  
551 from which the carbonates precipitated (e.g., Wei et al., 2019). Lu et al. (2016) proposed a  
552 threshold of  $2.5 \mu\text{mol}/\text{mol}$  as the upper boundary of oxygen-depleted water.

553         The Martin Point carbonate  $\text{I}/(\text{Ca}+\text{Mg})$  ratios record a range from 0.02 to 0.48  
554  $\mu\text{mol}/\text{mol}$  (Table 1, Fig. 5) and are lower than those recorded by the expanded Proterozoic  
555 marine anoxia ( $\sim 0.5\text{--}1.0 \mu\text{mol}/\text{mol}$ ). Similar low  $\text{I}/(\text{Ca}+\text{Mg})$  ratios have been also  
556 documented in Palaeozoic carbonate successions recording expansion of anoxia such as those  
557 from the Lower Ordovician and also Silurian on Laurentia that yielded ratios within the range  
558 of 0 and  $0.5 \mu\text{mol}/\text{mol}$  (Edwards et al., 2018; Young et al., 2019; Li and Azmy, 2023).  
559 Modern  $\text{I}/(\text{Ca}+\text{Mg})$  concentrations in sea surface waters above oxygen minimum zones (Rue  
560 et al., 1997), which represent current low oxygen settings, vary between 0 and  $2.5 \mu\text{mol}/\text{mol}$   
561 in contrast to values around  $5 \mu\text{mol}/\text{mol}$  for well-oxygenated conditions (Lu et al., 2016). The  
562 V and Mo concentrations are also consistent with the relatively reducing conditions reflected  
563 by the Martin Point  $\text{I}/(\text{Ca}+\text{Mg})$  ratios.

564         The Great Oxygenation Event of the Precambrian had values near  $2 \mu\text{mol}/\text{mol}$   
565 (Hardisty et al., 2014), reasonably far above those of the Martin Point carbonates and it is  
566 noteworthy that the Proterozoic was an eon with relatively low oxygen. The magnitudes of

567 the peaks in the Martin Point profile (Fig. 5) are similar to those of previous studies, which  
568 indicated local redox variations within dominant conditions of low  $I/(Ca+Mg)$  ratios (e.g.,  
569 Bowman et al., 2021). Therefore, the values are consistent with the dysoxic slope-  
570 environment conditions that were suggested by earlier sedimentological studies (e.g., James  
571 and Steven, 1986; Landing, 2012, 2013; Terfelt et al., 2014; Landing and Webster, 2018) and  
572 support not only a relatively reducing water column caused by transgression but also the  
573 consequent inhibition of primary productivity (lack of bioturbation). Thus, the eastern  
574 Laurentian continental margin was likely under poorly oxygenated seawaters and an  
575 expanded oxygen minimum zone due to inhibited ocean circulation that was driven by  
576 dominant Late Cambrian greenhouse climates (e.g., Erlick et al., 2011; Landing 2012).

## 577 7. Conclusions

578 Petrographic and geochemical screening support the preservation of at least near-  
579 primary signatures of the Zn-isotopes,  $I/(Ca+Mg)$  ratios, and trace elements retained in the  
580 Upper Cambrian lime mudstones of the toe-of-slope rhythmites at Martin Point, western  
581 Newfoundland. The signatures are therefore reliable proxies to reconstruct and study the  
582 paleoenvironmental conditions during the Late Cambrian.

583 The profiles of trace elements and  $I/(Ca+Mg)$  ratios exhibit consistent variations in  
584 association with the previously studied global negative  $\delta^{13}C_{carb}$  shifts of NL1, NL2, and  
585 HERB events. The  $\delta^{66}Zn$  values along the profile show little variations and the average  $\delta^{66}Zn$   
586 value of carbonates is  $0.33 \pm 0.12\%$ , which is within the range of modern seawater value.  
587 However, minor decreases in  $\delta^{66}Zn$  values are consistent with a decrease in primary  
588 productivity during dysoxic conditions.

589 The positive shifts in the TOC, and Ca-normalized P, Ni, Cu, Mn, Fe, V, and Mo  
590 profiles at the stratigraphic levels correlated with the base of the events could reflect  
591 inhibition of bioproductivity caused by shoaling organic-rich anoxic waters during

592 transgression. The Al/Ti ratios consistently point to correlated humid and warm climate  
593 periods.

594 The low I/(Ca+Mg) ratios support dominant dysoxic conditions along the entire  
595 section and are consistent with sea transgression and a warm humid climate context. The  
596 Mn/Al, Fe/Al, V, and Mo proxies reinforce the dysoxic conditions scenario.

## 597 **Acknowledgment**

598 The authors want to thank two anonymous reviewers for their constructive reviews.  
599 Also, the efforts of Dr. Xioamin Zhu (associate editor) are much appreciated. Special thanks  
600 to Dr. Svend Stouge for his help with the fieldwork and Mr. Niraj Shukla (MITACS). This  
601 project was supported by funding (to Karem Azmy) from MITACS and the Petroleum  
602 Exploration Enhancement Program (PEEP), NL, Canada.

## 603 **List of Figures and Tables**

604 **Fig. 1.** Location map of the study area illustrating (a) the general location of Newfoundland  
605 in eastern Canada, (b) the study area of the Martin Point section in western Newfoundland  
606 and surface geology, (c) a closeup of (b) with the location of the Martin Point section (49°  
607 40' 51" N, 57° 57' 36" W) (adapted from James and Stevens, 1986; Cooper et al., 2001), and  
608 (d) a simplified paleogeographic reconstruction with the approximate locations of the Martin  
609 Point (western Newfoundland) and Wa'ergang (South China) sections during Late Cambrian  
610 (modified from Blakey, 2008; Gill et al., 2021).

611 **Fig. 2.** Stratigraphic framework of the investigated carbonates in western Newfoundland,  
612 showing the  $\delta^{13}\text{C}$  profiles, positions of the samples and conodont zonation scheme (Barnes,  
613 1988; Li et al., 2017; Stitt, 1977) for (a) post-SPICE (from Azmy, 2019b) and HERB  
614 intervals (from Azmy, 2019a; Wang and Azmy, 2020) and (b) global C-isotope profile of the  
615 Upper Cambrian (after Gradstein et al., 2020; Zhao et al., 2022), on which the correlated

616 post-SPICE (N1 and N2) and HERB negative  $\delta^{13}\text{C}$  shifts of the Wa'ergang section (Li et al.,  
617 2017) are marked. The circles mark the correlated negative excursions. Numerical ages are  
618 from Schmid (2017).

619 **Fig. 3.** Photomicrographs of the preserved micritic fabric of the studied lime mudstones  
620 displaying (a) plane polarized (PL) image of Sample B31-1 from the lower Martin Point  
621 section (post-SPICE, Appendix 1), (b) CL image (non-CL) of (a), (c) plane polarized (PL)  
622 image of Sample MH5 from from the upper Martin Point section (HERB, Appendix 1), and  
623 (d) CL image (dull CL) of (c).

624 **Fig. 4.** Scatter diagrams showing the correlations of Sr with (a)  $\delta^{13}\text{C}$ , (b)  $\text{I}/(\text{Ca}+\text{Mg})$ , (c) P,  
625 (d) Ni, (e) Zn, (f)  $\delta^{66}\text{Zn}$ , (g) Al, (h)  $\Sigma\text{REE}$ , (i) Mn, (j) Fe, (k) V, (l) U, (m) Th/U, and (n)  
626  $\text{I}/(\text{Ca}+\text{Mg})$  with TOC for the carbonates spanning the post-SPICE (red dots) and HERB  
627 (black dots) events in the Martin Point section.

628 **Fig. 5.** Profiles of TOC,  $\delta^{66}\text{Zn}$ ,  $\text{I}/(\text{Ca}+\text{Mg})$ , Zn, Sr, P, Ni, Cu, Al/Ti, Mn, Fe, V, Mo, and  
629 Th/U, for post-SPICE and HERB, the elemental proxies are normalized to Ca. The  $\delta^{13}\text{C}$   
630 profile is reproduced from Azmy (2019a,b). The TOC data of HERB are derived from Wang  
631 and Azmy (2020) and post-SPICE from Okafor and Azmy (2024).

632 **Table 1.** Statistics of isotopic and elemental geochemistry of the investigated carbonates  
633 from the lower (post-SPICE) and upper (HERB) Martin Point section. The highlighted values  
634 are from Wang and Azmy (2020) and the TOC data of the lower Martin Point section,  
635 spanning the post-SPICE event, from Okafor and Azmy (2024).

636 **Appendix 1.** Elemental and isotopic geochemical compositions of the investigated  
637 carbonates from the Martin Point section in western Newfoundland. The highlighted values  
638 are from Wang and Azmy (2020). The  $\delta^{13}\text{C}$  and  $\delta^{18}\text{O}$  profiles are reproduced from Azmy

639 (2019a, b) and the TOC data of the lower Martin Point section, spanning the post-SPICE  
640 event, from Okafor and Azmy (2024).

## 641 **References**

- 642 Acharya, S.S., Panigrahi, M.K., Gupta, A.K., Tripathy, S., 2015. Response of trace metal  
643 redox proxies in continental shelf environment: The Eastern Arabian Sea scenario.  
644 *Continental Shelf Research*, 106, 70-84.
- 645 Allen, J.S., Thomas, W.A., Lavoie, D., 2010. The Laurentian margin of northeastern North  
646 America. *The Geological Society of America, Memoir* 206, 71-90.
- 647 Algeo, T. J., & Li, C. (2020). Redox classification and calibration of redox thresholds in  
648 sedimentary systems. *Geochimica et Cosmochimica Acta*, 287, 8–26.
- 649 Algeo, T. J., Maynard, J. B., 2004. Trace-element behaviour and redox facies in core shales  
650 of Upper Pennsylvanian Kansas-type cyclothems. *Chemical Geology* 206, 289-318.
- 651 Algeo, T. J., Tribovillard, N., 2009. Environmental analysis of paleoceanographic systems  
652 based on molybdenum-uranium covariation. *Chemical Geology* 268, 211-225.
- 653 Anbar, A. D., Duan, Y., Lyons, T. W., Arnold, G. L., Kendall, B., Creaser, R. A., Kaufman,  
654 A. J., Gordon, G. W., Scott, C., Buick, R., 2007. A whiff of oxygen before the Great  
655 Oxidation Event? *Science* vol. 317, issue 5846, 1903-1906.
- 656 Andersen, M. B., Vance, D., Archer, C., Anderson, R. F., Ellwood, M. J., Allen, C. S., 2011.  
657 The Zn abundance and isotopic composition of diatom frustules, a proxy for Zn availability  
658 in ocean surface seawater. *Earth and Planetary Science Letters*, 301(1-2), 137-145.
- 659 Archer, C., Andersen, M.B., Cloquet, C., Conway, T.M., Dong, S., Ellwood, M., Moore, R.,  
660 Nelson, J., Rehkämper, M., Rouxel, O., Samanta, M., 2017. Inter-calibration of a proposed  
661 new primary reference standard AA-ETH Zn for zinc isotopic analysis. *Journal of Analytical*  
662 *Atomic Spectrometry*, 32(2), 415-419.
- 663 Azmy, K., 2019a. Carbon-isotope stratigraphy of the uppermost Cambrian in eastern  
664 Laurentia: implications for global correlation. *Geological Magazine* 156 (5), 2019, 759–771.
- 665 Azmy, K., 2019b. Carbon-isotope stratigraphy of the SPICE event (Upper Cambrian) in  
666 eastern Laurentia: implications for global correlation and a potential reference section.  
667 *Geological Magazine* 156, 1311–1322.
- 668 Azmy, K., Brand, U., Sylvester, P. Gleeson, S.A., Logan, A., Bitner, M.A., 2011. Biogenic  
669 and abiogenic low-Mg calcite (bLMC and aLMC): Evaluation of seawater-Ree composition,  
670 water masses and carbonate diagenesis. *Chemical Geology* 280, 180-190.
- 671 Babcock, L.E., Peng, S.C., Brett, C.E., Zhu, M.Y., Ahlberg, P., Bevis, M., Robison, R.A.,  
672 2015. Global climate, sea level cycles, and biotic events in the Cambrian Period.  
673 *Palaeoworld*, 24(1-2), 5-15.
- 674 Bagnoli, G., Barnes, C.R., Stevens, R.K., 1986. Lower Ordovician (Tremadocian) conodonts  
675 from Broom Point and Green Point, Western Newfoundland. *Bollettino della Società*  
676 *Paleontologica Italiana*, 25(2), 145-158 (printed in 1987).

- 677 Barnes, C.R., 1988. The proposed Cambrian-Ordovician global boundary stratotype and point  
678 (GSSP) in Western Newfoundland, Canada. *Geol. Mag.* 125 (4). 1988, 381-414.
- 679 Bau, M., Dulski, P., 1996. Distribution of yttrium and rare-earth elements in the Penge and  
680 Kuruman iron-formations, Transvaal Supergroup, South Africa. *Precambrian Research* 79,  
681 37-55.
- 682 Bengtson, S., Sallstedt, T., Belivanova, V. and Whitehouse, M., 2017. Three-dimensional  
683 preservation of cellular and subcellular structures suggests 1.6 billion-year-old crown-group  
684 red algae. *PLoS Biology*, 15(3), p.e2000735.
- 685 Bermin, J., Vance, D., Archer, C., Statham, P. J., 2006. The determination of the isotopic  
686 composition of Cu and Zn in seawater. *Chem. Geol.* 226 (3–4), 280–297.
- 687 Bouma, A.H., 1962. *Sedimentology of some flysch deposits*. Elsevier, Amsterdam, 168.
- 688 Böning, P., Brumsack, H-J., Schnetger, B., Grunwald, M., 2009. Trace element signatures of  
689 Chilean upwelling sediments at ~ 36°S. *Marine Geology*, 259 (1-4), 112-121.
- 690 Bowman, C.N., Them, T.R., Knight, M.D., Kaljo, D., Eriksson, M.E., Hints, O., Martma, T.,  
691 Owens, J.D., Young, S.A., 2021. A multi-proxy approach to constrain reducing conditions in  
692 the Baltic Basin during the late Silurian Lau carbon isotope excursion. *Palaeogeography*,  
693 *Palaeoclimatology*, *Palaeoecology* 581, 110624.
- 694 Boyle, E.A., John, S., Abouchami, W., Adkins, J. F., Echegoyen-Sanz, Y., Ellwood, M.,  
695 Flegal, A. R., Fornace, K., Gallon, C., Galer, S., Gault-Ringold, M., Lacan, F., Radic, A.,  
696 Rehkamper, M., Rouxel, O., Sohrin, Y., Stirling, C., Thompson, C., Vance, D., Xue, Z. C.,  
697 Zhao, Y., 2012. GEOTRACES IC1 (BATS) contamination-prone trace element isotopes Cd,  
698 Fe, Pb, Zn, Cu, and Mo intercalibration. *Limnology and Oceanography-Methods*, 10, 653-  
699 665
- 700 Breit, G.N., Wanty, R.B., 1991. Vanadium accumulation in carbonaceous rocks: a review of  
701 geochemical controls during deposition and diagenesis. *Chemical Geology*, 91(2), 83-97.
- 702 Broecker, W.S., Peng, T.H., 1982. *Tracers in the Sea*. Eldigio, Pallisades, NY, 690.
- 703 Bruland, K.W., 1980. Oceanographic distributions of cadmium, zinc, nickel and copper in the  
704 North Pacific. *Earth and Planetary Science Letters* 47, 176-198.
- 705 Brumsack, H.J., Gieskes, J. M., 1983. Interstitial water trace-metal chemistry of laminated  
706 sediments from the Gulf of California, Mexico. *Marine Chemistry*, 14(1), 89-106.
- 707 Cawood, P.A., McCausland, P.J.A., Dunning, G.R., 2001. Opening Iapetus: Constraints from  
708 the Laurentian margin in Newfoundland. *GSA Bulletin* v. 113, No. 4, 443–453.
- 709 Canfield, D.E., 1993. Organic Matter Oxidation in Marine Sediments. In: Wollast, R.,  
710 Mackenzie, F.T., Chou, L. (eds) *Interactions of C, N, P and S Biogeochemical Cycles and*  
711 *Global Change*. NATO ASI Series, vol 4. Springer, Berlin, Heidelberg.
- 712 Canfield, D.E., 1994. Factors influencing organic carbon preservation in marine sediments.  
713 *Chemical Geology* 114, 315-329.
- 714 Chen, D., Qing, H., Li, R., 2005. The Late Devonian Frasnian–Famennian (F/F) biotic crisis:  
715 Insights from  $\delta^{13}\text{C}_{\text{carb}}$ ,  $\delta^{13}\text{C}_{\text{org}}$  and  $87\text{Sr} / 86\text{Sr}$  isotopic systematics. *Earth and Planetary*  
716 *Science Letters* 235 (1-2), 151-166.

- 717 Chen, X., Sageman, B.B., Yao, H., Liu, S.A., Han, K., Zou, Y., Wang, C., 2021. Zinc isotope  
718 evidence for paleoenvironmental changes during Cretaceous Oceanic Anoxic Event 2.  
719 *Geology*, 49(4), 412-416.
- 720 Cheng, M., Li, C., Zhou, L., Feng, L., Algeo, T.J., Zhang, F., Romaniello, S., Jin, C., Ling,  
721 H. and Jiang, S., 2017. Transient deep-water oxygenation in the early Cambrian Nanhua  
722 Basin, South China. *Geochimica et Cosmochimica Acta*, 210, pp.42-58.
- 723 Clarkson, M.O., Poulton, S.W., Guilbaud, R., Wood, R.A., 2014. Assessing the utility of  
724 Fe/Al and Fe-speciation to record water column redox conditions in carbonate-rich  
725 sediments. *Chemical Geology*, 382, 111-122.
- 726 Coniglio, M., 1985. Origin and diagenesis of fine-grained slope sediments: Cow Head Group  
727 (Cambro-Ordovician), western Newfoundland. Doctoral (PhD) thesis, Memorial University  
728 of Newfoundland.
- 729 Conway, T. M., Rosenberg, Angela D., Adkins, J. F., John, S. G., 2013. A new method for  
730 precise determination of iron, zinc and cadmium stable isotope ratios in seawater by double-  
731 spike mass spectrometry. *Analytica Chimica Acta*, 793(0), 44-52.  
732
- 733 Conway, T., John, S.G., 2014. The biogeochemical cycling of zinc and zinc isotopes in the  
734 North Atlantic Ocean. *Global Biogeochemical Cycles*, 28(10), 1111-1128.  
735
- 736 Conway, T., John, S.G., 2015. The cycling of iron, zinc and cadmium in the North East  
737 Pacific Ocean – Insights from stable isotopes. *Geochimica et Cosmochimica Acta*, 164(0),  
738 262-283  
739
- 740 Cooper, R.A., Nowlan, G.S., Williams, S.H., 2001. Global Stratotype Section and Point for  
741 the base of the Ordovician System. *Episodes* 24, 19-28.
- 742 Cousineau, P.A., Tremblay, A., 1993. Acadian deformations in the southwestern Quebec  
743 Appalachians. In *The Acadian Orogeny*. Edited by D.C. Roy and J.W. Skehan. Geological  
744 Society of America, Special Paper 275, pp. 85–99.
- 745 D’Arcy, J., Gilleaudeau, G.J, Peralta, S., Gaucher, C., Frei, R. 2017. Redox fluctuations in  
746 the Early Ordovician oceans: An insight from chromium stable isotopes. *Chemical Geology*,  
747 volume 448, 1-12.
- 748 Dickson, J.A.D., 1966. Carbonate identification and genesis as revealed by staining. *Journal*  
749 *of Sedimentary Research*, 36(2), 491–505.
- 750 Dolenc, T., Lojen, S. and Ramovš, A., 2001. The Permian-Triassic boundary in Western  
751 Slovenia (Idrijca Valley section): magnetostratigraphy, stable isotopes, and elemental  
752 variations. *Chemical Geology* 175, 175-190.
- 753 Dunham, R.J., 1962. Classification of Carbonate Rocks According to Depositional Texture.  
754 *In: Ham, W.E., Ed., Classification of Carbonate Rocks*, AAPG, Tulsa, 108-121.
- 755 Edwards, C.T., Fike, D.A., Saltzman, M.R., Lu, W. and Lu, Z., 2018. Evidence for local and  
756 global redox conditions at an Early Ordovician (Tremadocian) mass extinction. *Earth and*  
757 *Planetary Science Letters* 481, 125-135.
- 758 Elderfield, H., Truesdale, V.W., 1980. On the biophilic nature of iodine in seawater. *Earth*  
759 *and Planetary Science Letters*, 50(1), 105-114.

- 760 Emerson, S.R., Huested, S.S., 1991. Ocean anoxia and the concentrations of molybdenum  
761 and vanadium in seawater. *Mar. Chem.* 34, 177–196.
- 762 Fantle, M. S., Barnes, B.D., Lau, K.V., 2020. The role of diagenesis in shaping the  
763 geochemistry of the marine carbonate record. *Annu. Rev. Earth Planet. Sci.* 48:549-83.
- 764 Feng, X., Redfern, S.A., 2018. Iodate in calcite, aragonite and vaterite CaCO<sub>3</sub>: Insights from  
765 first-principles calculations and implications for the I/Ca geochemical proxy. *Geochimica et*  
766 *Cosmochimica Acta*, 236, pp.351-360.
- 767 Fuge, R., Johnson, C.C. 1986. The geochemistry of iodine—a review. *Environ. Geochem.*  
768 *Health* 8, 31–54.
- 769 Gao, P., Liu, G., Jia, C., Young, A., Wang, Z., Wang, T., Zhang, P., Wang, D., 2016. Redox  
770 variations and organic matter accumulation on the Yangtze carbonate platform during Late  
771 Ediacaran–Early Cambrian: constraints from petrology and geochemistry. *Palaeogeography,*  
772 *Palaeoclimatology, Palaeoecology*, 450, 91-110.
- 773 Gao, Y., Zhang, X., Xu, Y., Fang, C., Gong, Y., Shen, Y., 2020. High primary productivity  
774 during the Ediacaran Period revealed by the covariation of paired C-isotopic records from  
775 South China. *Precambrian Research*, 349, 105411.
- 776 German, C.R., Elderfield, H., 1990. Application of the Ce anomaly as a paleoredox indicator:  
777 the ground rules. *Paleoceanography* 5, 823-833.
- 778 Gill, B.C., Lyons, T.W., Young, S.A., Kump, L.R., Knoll, A.H., Saltzman, M. R., 2011.  
779 Geochemical evidence for widespread euxinia in the Later Cambrian ocean. *Nature* 469, 80-  
780 83.
- 781 Gradstein, F.M., Ogg, J.G., Schmitz, M.D., Ogg, G.M. eds., 2020. *Geologic Time Scale*  
782 2020. Elsevier, Amsterdam, Netherlands, 2020.
- 783 Hardisty, D.S., Lu, Z., Bekker, A., Diamond, C.W., Gill, B.C., Jiang, G., Kah, L.C., Knoll,  
784 A.H., Loyd, S.J., Osburn, M.R., Planavsky, N.J., 2017. Perspectives on Proterozoic surface  
785 ocean redox from iodine contents in ancient and recent carbonate. *Earth and Planetary*  
786 *Science Letters*, 463, 159-170.
- 787 Hardisty, D.S., Lu, Z., Planavsky, N.J., Bekker, A., Philippot, P., Zhou, X., Lyons, T.W.,  
788 2014. An iodine record of Paleoproterozoic surface ocean oxygenation. *Geology*, 42(7), 619-  
789 622.
- 790 Hayes, C. T., Anderson, R. F., Cheng, H., Conway, T. M., Edwards, R. L., Fleisher, M. Q.  
791 Ho, P., Huang, K-F., John, S. G., Landing, W. M., Little, S. H., Lu, Y., Morton, P. L.,  
792 Moran, S. B., Robinson, L. F., Shelley, R. U., Shiller, A. M., Zheng, X-Y., 2017.  
793 Replacement Times of a Spectrum of Elements in the North Atlantic Based on Thorium  
794 Supply. *Global Biogeochemical Cycles*, 32(9), 1294-1311.
- 795 Hashim, M.S., Burke, J.E., Hardisty, D.S. and Kaczmarek, S.E., 2022. Iodine incorporation  
796 into dolomite: Experimental constraints and implications for the iodine redox proxy and  
797 Proterozoic Ocean. *Geochimica et Cosmochimica Acta*, 338, 365-381.
- 798 He, R., Lu, W., Junium, C.K., Ver Straeten, C.A., Lu, Z., 2020. Paleo-redox context of the  
799 mid-Devonian Appalachian basin and its relevance to biocrises. *Geochem. Cosmochim. Acta*  
800 287, 328–340.

- 801 Hetzel, A., Böttcher, M.E., Wortmann, U.G., Brumsack, H.J., 2009. Paleo-redox conditions  
802 during OAE 2 reflected in Demerara Rise sediment geochemistry (ODP Leg  
803 207). *Palaeogeography, Palaeoclimatology, Palaeoecology*, 273(3-4), pp.302-328.
- 804 Hohl, S.V., Becker, H., Herzlieb, S., Guo, Q., 2015. Multiproxy constraints on alteration and  
805 primary compositions of Ediacaran deep-water carbonate rocks, Yangtze Platform, South  
806 China. *Geochimica et Cosmochimica Acta* 163, 262-278.
- 807 Horner, T. J., Little, S. H., Conway, T. M., Farmer, J. R., Hertzberg, J. E., Janssen, D. J.,  
808 Lough, A. J. M., McKay, J. L., Tessin, A., Galer, S. J. G., Jaccard, S. L., Lacan, F., Paytan,  
809 A., Wuttig, K., 2021. Bioactive Trace Metals and Their Isotopes as Paleoproductivity  
810 Proxies: An Assessment Using GEOTRACES-Era Data. *Global Biogeochemical Cycles*,  
811 35(11), e2020GB006814.
- 812  
813 Hu, Q., Zhao, P., Moran, J. E., Seaman, J.C., 2005. Sorption and transport of Iodine species  
814 in sediments from the Savannah River and Hanford Sites. *J. Contam. Hydrol.*, 78, 185-205.
- 815 James, N.P., Stevens, P.K., 1986. Stratigraphy and correlation of the Cambro-Ordovician  
816 Cow Head Group, western Newfoundland. *Geological Survey of Canada Bulletin* 366, 1–  
817 143.
- 818 James, N.P., Stevens, R.K., Barnes, C.R., Knight, I., 1989. A lower Paleozoic continental  
819 margin carbonate platform, northern Canadian Appalachians. *In: Crevello P.D., Wilson J.L.,*  
820 *Sarg J.F. and Read J.F. (eds) Controls on Carbonate Platform and Basin Development.*  
821 *Society of Economic Palaeontologists and Mineralogists, Special Publications*, 44, 123- 146.
- 822 Jin, C., Li, C., Algeo, T.J., O'Connell, B., Cheng, M., Shi, W., Shen, J. and Planavsky, N.J.,  
823 2018. Highly heterogeneous “poikiloredox” conditions in the early Ediacaran Yangtze  
824 Sea. *Precambrian Research*, 311, pp.157-166.
- 825 John, S.G., Conway, T.M., 2014. A role for scavenging in the marine biogeochemical cycling  
826 of zinc and zinc isotopes. *Earth Planet. Sci. Lett.* 394, 159–167.
- 827 John, S.G., Helgoe, J., Townsend, E., 2018. Biogeochemical cycling of Zn and Cd and their  
828 stable isotopes in the Eastern Tropical South Pacific. *Marine Chemistry*, 201, 256-262.
- 829 Kasemann, S.A., Schmidt, D.N., Bijma, J., Foster, G.L., 2009. In situ boron isotope analysis  
830 in marine carbonates and its application for foraminifera and palaeo-pH. *Chemical Geology*  
831 volume 260, issues 1-2, 138-147.
- 832 Kindle, C.H., Whittington, H.B., 1958. Stratigraphy of the Cow Head region, western  
833 Newfoundland. *GSA Bulletin* 69 (3), 315-342.
- 834 Köbberich, M. and Vance, D., 2019. Zn isotope fractionation during uptake into marine  
835 phytoplankton: Implications for oceanic zinc isotopes. *Chemical Geology*, 523, 154-161.
- 836 Kunzmann, M., Halverson, G.P., Sossi, P.A., Raub, T.D., Payne, J.L., Kirby, J., 2013. Zn  
837 isotope evidence for immediate resumption of primary productivity after snowball Earth.  
838 *Geology* 41 (1), 27–30.
- 839 Lacombe, R.A., Waldron, J.W.F., Williams, S.H., Harris, N.B., 2019. Melanges and  
840 disrupted rocks at the leading edge of the Humber Arm Allochthon, W. Newfoundland  
841 Appalachians: Deformation under high fluid pressure. *Gondwana Research* 74, 216-236.

- 842 Landing, E., 2012. Time-specific black mudstones and global hyperwarming on the  
843 Cambrian–Ordovician slope and shelf of the Laurentia. *Palaeogeography, Palaeoclimatology,*  
844 *Palaeoecology*, 367–368, 256–272.
- 845 Landing, E., 2013. The Great American Carbonate Bank in northeast Laurentia: Its births,  
846 deaths, and linkage to continental slope oxygenation (Early Cambrian–Late Ordovician).  
847 *American Association of Petroleum Geologists Bulletin, Memoir*, 98, 451–492.
- 848 Landing, E., Webster, M., 2018. Iapetan rift–passive margin transition in NE Laurentia and  
849 eustatic control on continental slope oxygenation, Taconic slate colors, and Early Paleozoic  
850 climate. *Guidebook the Field Trips in New York, Vermont, and Massachusetts*.
- 851 Lawrence, M.G., Greig, A., Collerson, K.D., Kamber, B.S., 2006. Rare earth element and  
852 yttrium variability in South East Queensland waterways. *Aquatic Geochemistry*, 12, 39–72.
- 853 Lemaitre, N., de Souza, G. F., Archer, C., Wang, R-M., Planquette, H., Sarthou, G., Vance,  
854 D., 2020. Pervasive sources of isotopically light zinc in the North Atlantic Ocean. *Earth and*  
855 *Planetary Science Letters*, 539, 116216.
- 856 Leverenz, H.W., 1950. *Introduction to the Luminescence of Solids*. Wiley, New York, 340.
- 857 Li, X., Jenkyns, H.C., Wang, C., Hu, X., Chen, X., Wei, Y., Huang, Y., Cui, J., 2006. Upper  
858 Cretaceous carbon- and oxygen-isotope stratigraphy of hemipelagic carbonate facies from  
859 southern Tibet, China. *Journal of the Geological Society, London* 163, 375–82.
- 860 Li, D., Zhang, X., Chen, K., Zhang, G., Chen, X., Huang, W., Peng, S., Shen, Y., 2017. High-  
861 resolution C-isotope chemostratigraphy of the uppermost Cambrian stage (Stage 10) in South  
862 China: implications for defining the base of Stage 10 and palaeoenvironmental change.  
863 *Geological Magazine* 154, 1232–43.
- 864 Li, D., Zhang, X., Zhang, X., Zhu, H., Peng, S., Sun, L., Shen, Y., 2020. A paired carbonate-  
865 organic  $\delta^{13}\text{C}$  approach to understanding the Cambrian Drumian carbon isotope excursion  
866 (DICE). *Precambrian Research* 349, 105503.
- 867 Li, J., Azmy, K., Kendall, B., 2022. The Mo- and U-isotope signatures in alternating shales  
868 and carbonate beds of rhythmites: A comparison and implications for redox conditions across  
869 the Cambrian-Ordovician boundary. *Chemical Geology* 602, 120882.
- 870 Li, J., Azmy, K., 2023. Expanded marine anoxia at the Cambrian-Ordovician transition:  
871 Evidence from lime mudstones I/Ca and  $\delta^{238}\text{U}$  signatures of the GSSP in western  
872 Newfoundland, Canada. *Marine and Petroleum Geology* 155, 106408.
- 873 Liao, W.-H., Takano, S., Yang, S.-C., Huang, K.-F., Sohrin, Y. and Ho, T.-Y., 2020. Zn  
874 Isotope Composition in the Water Column of the Northwestern Pacific Ocean: The  
875 Importance of External Sources. *Global Biogeochemical Cycles* (34), e2019GB006379.
- 876 Liao, Z., Hu, W., Cao, J., Wang, X., & Fu, X., 2020. Oceanic anoxia through the late Permian  
877 Changhsingian Stage in the Lower Yangtze region, South China: Evidence from sulfur  
878 isotopes and trace elements. *Chemical Geology*, 532, 119371.
- 879 Ling, H.F., Chen, X., Li, D.A., Wang, D., Shields-Zhou, G.A. and Zhu, M., 2013. Cerium  
880 anomaly variations in Ediacaran–earliest Cambrian carbonates from the Yangtze Gorges area,  
881 South China: implications for oxygenation of coeval shallow seawater. *Precambrian*  
882 *Research*, 225, pp.110–127.

- 883 Liss, P.S., Herring, J.R., Goldberg, E.D., 1973. Iodide-iodate system in seawater as a possible  
884 measure of redox potential: *Nature Physical Science*, 242, 108–109.
- 885 Little, S.H., Vance, D., Walker-Brown, C., Landing, W.M., 2014 The oceanic mass balance  
886 of copper and zinc isotopes, investigated by analysis of their inputs, and outputs to  
887 ferromanganese oxide sediments. *Geochim. Cosmochim. Acta* 125, 673–693.
- 888 Little, S.H., Wilson, D.J., Rehkämper, M., Adkins, J.F., Robinson, L.F., van de Flierdt, T.,  
889 2021. Cold-water corals as archives of seawater Zn and Cu isotopes. *Chemical Geology*, 578,  
890 120304.
- 891 Liu, S.-A., Wu, H., Shen S.-z., Jiang, G., Zhang, S., Lv, Y., Zhang, H., Li, S., 2017. Zinc  
892 isotope evidence for intensive magmatism immediately before the end-Permian mass  
893 extinction. *Geology*, 45 (4), 343-346.
- 894 Lu, W., Barbosa, C.F., Rathburn, A.E., da Matta Xavier, P., Cruz, A.P.S., Thomas, E.,  
895 Rickaby, R.E.M, Zhang, Y.G., Lu, Z., 2021. Proxies for paleo-oxygenation: A downcore  
896 comparison between benthic foraminiferal surface porosity and I/Ca. *Palaeogeography,*  
897 *Palaeoclimatology, Palaeoecology* 579, 110588.
- 898 Lu, W., Wörndle, S., Halverson, G.P., Zhou, X., Bekker, A., Rainbird, R. H., Hardisty, D. S.,  
899 Lyons, T. W., Lu, Z., 2017. Iodine proxy evidence for increased ocean oxygenation during  
900 the Bitter Springs Anomaly. *Geochem. Persp. Let.* (2017) 5, 53-57
- 901 Lu, Z., Hoogakker, B.A.A., Hillenbrand, C.-D., Zhou, X., Thomas, E., Gutchess, K.M., Lu,  
902 W., Jones, L., Rickaby, R.E.M., 2016. Oxygen depletion recorded in upper waters of the  
903 glacial Southern Ocean. *Nat Commun* 7, 11146.
- 904 Lu, Z., Jenkyns, H.C., Rickaby, R.E., 2010. Iodine to calcium ratios in marine carbonate as a  
905 paleo-redox proxy during oceanic anoxic events. *Geology* 38, 1107–1110.
- 906 Lv, Y., Liu, S.-A., Wu, H., Hohl, S.V., Chen, S., and Li, S., 2018. Zn-Sr isotope records of  
907 the Ediacaran Doushantuo Formation in South China: diagenesis assessment and  
908 implications. *Geochimica et Cosmochimica Acta*, 239, 330-345.
- 909 Machel, H.G., 2000. Application of cathodoluminescence to carbonate diagenesis.  
910 *Cathodoluminescence in geosciences*. Springer, Berlin, Heidelberg, 271-301.
- 911 Machel, H.G., Burton, E.A., 1991. Factors governing cathodoluminescence in calcite and  
912 dolomite, and their implications for studies of carbonate diagenesis.
- 913 Maréchal, C.N., Nicolas, E., Douchet, C., Albarede, F., 2000. Abundance of zinc isotopes as  
914 a marine biogeochemical tracer. *Geochemistry, Geophysics, Geosystems*, 1(5).
- 915 Maréchal, C.N., Télouk, P., Albarède, F., 1999. Precise analysis of copper and zinc isotopic  
916 compositions by plasma-source mass spectrometry. *Chemical geology*, 156(1–4), 251–  
917 273. McLennan, S.M., 2001. Relationships between the trace element composition of  
918 sedimentary rocks and upper continental crust. *Geochemistry, Geophysics, Geosystems*, 2(4).
- 919 Meyer, E.E., Quicksall, A.N., Landis, J.D., Link, P.K., Bostick, B.C., 2012. Trace and rare  
920 earth elemental investigation of a Sturtian cap carbonate, Pocatello, Idaho: evidence for ocean  
921 redox conditions before and during carbonate deposition. *Precambrian Research*, 192, 89–  
922 106.

- 923 Middelburg, J.J., Van der Weijden, C.H., Woittiez, J.R.W., 1988. Chemical processes  
924 affecting the mobility of major, minor and trace elements during weathering of granitic rocks.  
925 *Chemical Geology* 68, 253-273.
- 926 Miller, J.F., Evans, K.R., Freeman, R.L., Ripperdan, R.L. Taylor, J.F., 2011. Proposed  
927 stratotype for the base of the Lawsonian Stage (Cambrian Stage 10) at the first appearance  
928 datum of *Eoconodontus notchpeakensis* (Miller) in the House Range, Utah, USA. *Bulletin of*  
929 *Geosciences* 86, 595–620.
- 930 Miller, J.F., Evans, K.R., Loch, J.D., Ethington, R.L., Stitt, J.H., Holmer, L.E., Popov, L.E.  
931 2003. Stratigraphy of the Sauk III interval (Cambrian–Ordovician) in the Ibex area, western  
932 Millard County, Utah. *Brigham Young University Geology Studies* 47, 23–118.
- 933 Millero, F.J., 1996. *Chemical Oceanography*. CRC Press, Boca Raton, FL, 496.
- 934 Morel, F.M.M., Reinfelder, J.R., Chamberlain, C.P., Roberts, S.B., Lee, J.G., Yee, D., 1994.  
935 Zinc and carbon co-limitation of marine phytoplankton. *Nature* 369, 740–742.
- 936 Morrison, J.O., Brand, U., 1986. Geochemistry of recent marine invertebrates. *Geoscience*  
937 *Canada*, 13, 237–253.
- 938 Müsing, K., Clarkson, M. O., Vance, D., 2022. The meaning of carbonate Zn isotope records:  
939 Constraints from a detailed geochemical and isotope study of bulk deep-sea carbonates.  
940 *Geochimica et Cosmochimica Acta*, 324, 26-43.
- 941 Muramatsu, Y., Wedepohl, K.H., 1998. The distribution of iodine in the earth's crust.  
942 *Chemical Geology*, 147(3-4), 201-216.
- 943 Nakada, R., Takahashi, Y., Tanimizu, M., 2013. Isotopic and speciation study on cerium  
944 during its solid-water distribution with implication for Ce stable isotope as a paleo-redox  
945 proxy. *Geochimica et Cosmochimica Acta*, Volume 103, 49–62.
- 946 Niu, J., Huang, W. and Fei, L., 2018. Paleoenvironment in an Ordovician carbonate reservoir  
947 in southwestern of Tarin Basin, NW China: Evidence from stable isotopes. *Energy Sources,*  
948 *Part A: Recovery, Utilization, and Environmental Effects*, 41:16.
- 949 Okafor, M-M.C, Azmy, K., 2024. Redox conditions across the Upper Cambrian of eastern  
950 Laurentia: Implications from geochemical proxies. *Palaeogeography, Palaeoclimatology,*  
951 *Palaeoecology* 637, 111978.
- 952 Pattan, J.N., Mir, I.A., Parthiban, G., Karapurkar, S.G., Matta, V.M., Naidu, P.D., Naqvi,  
953 S.W.A., 2013. Coupling between suboxic condition in sediments of the western Bay of  
954 Bengal and southwest monsoon intensification: A geochemical study. *Chemical Geology,*  
955 343, 55–66.
- 956 Pichat, S., Douchet, C., Albarède, F., 2003. Zinc isotope variations in deep-sea carbonates  
957 from the eastern equatorial Pacific over the last 175 ka. *Earth and Planetary Science Letters*  
958 210, 167-178.
- 959 Podder, J., Lin, J., Sun, W., Botis, S.M., Tse, J., Chen, N., Hu, Y., Li, D., Seaman, J., Pan, Y.,  
960 2017. Iodate in calcite and vaterite: Insights from synchrotron X-ray absorption spectroscopy  
961 and first-principles calculations. *Geochimica et Cosmochimica Acta* 198, 218–228.
- 962 Pons, M.L., Fujii, T., Rosing, M., Quitté, G., Télouk, P. and Albarède, F., 2013. A Zn isotope  
963 perspective on the rise of continents. *Geobiology*, 11(3), pp.201-214.

- 964 Quinn, L.A., 1992. Foreland and trench slope basin sandstones of the Goose Tickle Group  
965 and Lower Head Formation, western Newfoundland. PhD thesis, Memorial University of  
966 Newfoundland, St John's, Newfoundland.
- 967 Quinn, L., Williams, S.H., Harper, D.A.T., Clarkson, E.N.K., 1999. Late Ordovician foreland  
968 basin fill: Long Point Group of onshore western Newfoundland. *Bulletin of Canadian*  
969 *Petroleum Geology*, vol. 47, No. 1, 63–80.
- 970 Reeder, R.J., Lamble, G.M., Northrup, P.A., 1999. XAFS study of the coordination and local  
971 relaxation around  $\text{Co}^{2+}$ ,  $\text{Zn}^{2+}$ ,  $\text{Pb}^{2+}$ , and  $\text{Ba}^{2+}$  trace elements. *Am. Miner.* 84, 1049–1060.
- 972 Rostovtseva, Y.V., Kuleshov, V.N., 2016. Carbon and oxygen stable isotopes in the middle-  
973 upper Miocene and lower Pliocene carbonates of the Eastern Paratethys (Kerch-Taman  
974 Region). *Palaeoenvironments and post-sedimentation changes. Lithology and Mineral*  
975 *Resources* 51, 333-346.
- 976 Rue, E.L., Smith, G.J., Cutter, G.A., Bruland, K W., 1997. The response of trace element  
977 redox couples to suboxic conditions in the water column. *Deep-Sea Res., Part 144*, 113–134.
- 978 Rühlemann, C., Frank, M., Hale, W., Mangini, A., Mulitza, S., Müller, P.J., Wefer, G., 1996.  
979 Late Quaternary productivity changes in the western equatorial Atlantic: Evidence from  
980  $^{230}\text{Th}$ -normalized carbonate and organic carbon accumulation rates. *Marine Geology*, 135(1-  
981 4), 127–152.
- 982 Rush, P.F., Chafetz, H.S., 1990. Fabric retentive, non-luminescent brachiopods as indicators  
983 of original  $\delta^{13}\text{C}$  and  $\delta^{18}\text{O}$  compositions: a test. *Journal of Sedimentary Petrology*, 60: 968–  
984 981.
- 985 Samanta, M., Ellwood, M. J., Sinoir, M., Hassler, C. S., 2017. Dissolved zinc isotope cycling  
986 in the Tasman Sea, SW Pacific Ocean. *Marine Chemistry*, 192, 1-12.
- 987 Schoepfer, S.D., Shen, J., Wei, H., Tyson, R.V., Ingall, E., Algeo, T.J., 2015. Total organic  
988 carbon, organic phosphorus, and biogenic barium fluxes as proxies for paleomarine  
989 productivity. *Earth-Science Reviews*, 149, pp.23-52.
- 990 Scholz, F., Siebert, C., Dale, A.W., Frank, M., 2017. Intense molybdenum accumulation in  
991 sediments underneath a nitrogenous water column and implications for the reconstruction of  
992 paleo-redox conditions based on molybdenum isotopes. *Geochimica et Cosmochimica Acta*  
993 volume 213, 400–417.
- 994 Shao, L., Cui, Y., Qiao, P., Zhang, D., Liu, X., Zhang, C., 2017. Sea-level changes and  
995 carbonate platform evolution of the Xisha Islands (South China Sea) since the Early Miocene.  
996 *Palaeogeography, Palaeoclimatology, Palaeoecology*, 485, 504–5016.
- 997 Śliwiński, M.G., Whalen, M.T., Jed, D.A.Y., 2010 Trace element variations in the Middle  
998 Frasnian Punctata Zone (Late Devonian) in the Western Canada sedimentary basin—changes  
999 in oceanic bioproductivity and paleoredox spurred by a pulse of terrestrial afforestation?  
1000 *Geologica Belgica* 13/4, 459–482.
- 1001 Schmid, S., 2017. Chemostratigraphy and palaeo-environmental characterization of the  
1002 Cambrian stratigraphy in the Amadeus Basin, Australia. *Chemical Geology*, 451, 169–182.
- 1003 Sieber, M., Conway, T. M., de Souza, G. F., Hassler, C. S., Ellwood, M. J., Vance, D., 2020.  
1004 Cycling of zinc and its isotopes across multiple zones of the Southern Ocean: Insights from

- 1005 the Antarctic Circumnavigation Expedition. *Geochimica et Cosmochimica Acta*, 268, 310-  
1006 324.
- 1007 Spokes, L.J., Liss, P.S., 1996. Photochemically induced redox reactions in seawater, II.  
1008 Nitrogen and iodine. *Marine chemistry*, 54(1-2), 1–10.
- 1009 Stenzel, S.R., Knight, I., James, N.P., 1990. Carbonate platform to foreland basin: Revised  
1010 stratigraphy of the Table Head Group (Middle Ordovician), western Newfoundland:  
1011 *Canadian Journal of Earth Sciences*, v. 27, 14–26.
- 1012 Stevens, R.K., 1970. Cambro-Ordovician flysch sedimentation and tectonics in west  
1013 Newfoundland and their possible bearing on a proto-Atlantic Ocean; *Flysch Sedimentology*  
1014 in North America, Geological Association of Canada, Special Paper 7, 165–177.
- 1015 Stitt, J. H., 1977. Late Cambrian and earliest Ordovician trilobites, Wichita Mountains,  
1016 Murray County, Oklahoma. *Oklahoma Geological Survey Bulletin* 124, 79.
- 1017 Stow, D., Shanmugam, G., 1980. Sequence of structures in fine-grained turbidites:  
1018 Comparison of recent deep-sea and ancient flysch sediments. *Sedimentary Geology*, 25, 23-  
1019 42.
- 1020 Stouge, S., Bagnoli, G., McIlroy, D., 2017. Cambrian–Middle Ordovician platform-slope  
1021 stratigraphy, palaeontology and geochemistry of western Newfoundland, Canada.  
1022 *International Symposium on the Ediacaran-Cambrian Transition, Field Trip 2*.
- 1023 Takano, S., Tanimizu, Masaharu, H., Takafumi, Shin, K.-C., Fukami, Y., Suzuki, K., Sohrin,  
1024 Y., 2017. A simple and rapid method for isotopic analysis of nickel, copper, and zinc in  
1025 seawater using chelating extraction and anion exchange. *Analytica Chimica Acta*, 967, 1-11.
- 1026 Taylor, S.R., McLennan, S.M., 1980. Rare earth element evidence for the chemical  
1027 composition of the Archaean crust. *Proc. 2nd Int. Archaean Symp.*, Perth, W.A. In:  
1028 McLennan, S.M., Nance, W.B. and Taylor, S.R., 1980. Rare earth element-thorium  
1029 correlations in sedimentary rocks, and the composition of the continental crust. *Geochimica*  
1030 *et Cosmochimica Acta*, 44(11), 1833-1839.
- 1031 Taylor, S.R., McLennan, S.M., 1985. *The continental crust: Its composition and evolution*.  
1032 Blackwell, Malden, Mass.
- 1033 Terfelt, F., Eriksson, M.E., Schmitz, B., 2014. The Cambrian-Ordovician transition in  
1034 dysoxic facies in Baltica – Diverse faunas and carbon isotope anomalies. *Palaeogeography,*  
1035 *Palaeoclimatology, Palaeoecology*, 394, 59–73.
- 1036 Togo, Y.S., Takahashi, Y., Amano, Y., Matsuzaki, H., Suzuki, Y., Terada, Y., Muramatsu,  
1037 Y., Ito, K., Iwatsuki, T., 2016. Age and speciation of iodine in groundwater and mudstones of  
1038 the Horonobe area, Hokkaido, Japan: implications for the origin and migration of iodine  
1039 during basin evolution. *Geochem. Cosmochim. Acta* 191, 165–186.
- 1040 Tostevin, R., Shields, G.A., Tarbuck, G.M., He, T., Clarkson, M.O. and Wood, R.A., 2016.  
1041 Effective use of cerium anomalies as a redox proxy in carbonate-dominated marine  
1042 settings. *Chemical Geology*, 438, pp.146-162.
- 1043 Tribouvillard, N., Algeo, T.J., Baudin, F., Riboulleau, A., 2012. Analysis of marine  
1044 environmental conditions based on molybdenum–uranium covariation—Applications to  
1045 Mesozoic paleoceanography. *Chemical Geology*, 324, 46–58.

- 1046 Truesdale, V.W., Bailey, G.W., 2000. Dissolved iodate and total iodine during an extreme  
1047 hypoxic event in the Southern Benguela system. *Estuarine, Coastal and Shelf Science*, 50(6),  
1048 751–760.
- 1049  
1050 Vance, D., Little, S. H., de Souza, G. F., Khatiwala, S., Lohan, M. C. and Middag, R., 2017.  
1051 Silicon and zinc biogeochemical cycles coupled through the Southern Ocean. *Nature*  
1052 *Geoscience*, 10(3), 202-206.
- 1053 Vance, D., de Souza, G. F., Zhao, Y., Cullen, J. T. and Lohan, M. C., 2019. The  
1054 relationship between zinc, its isotopes, and the major nutrients in the North-East Pacific.  
1055 *Earth and Planetary Science Letters*, 525, 115748.
- 1056  
1057 Veizer, J. 1983 Chemical diagenesis of carbonates: theory and application of trace elements  
1058 technique. In: Arthur, M.A., Anderson, T.F., Kaplan, I.R., Veizer, J., Land, L. S. (Eds.),  
1059 *Stable Isotopes in Sedimentary Geology*, vol. 10. Society of Economic Paleontologists and  
1060 Mineralogists (SEPM), Short Course Notes, pp. 3.1–3.100.
- 1061 Veizer, J., Ala, D., Azmy, K.; Bruckschen, P., Bruhn, F, Buhl, D. Carden, G., Diener, A.,  
1062 Ebner, S., Goddard, Y., Jasper, T., Korte, C., Pawellek, F., Podlaha, O., Strauss, H., 1999.  
1063  $^{87}\text{Sr}/^{86}\text{Sr}$ ,  $\delta^{18}\text{O}$  and  $\delta^{13}\text{C}$  evolution of Phanerozoic seawater. *Chemical Geology*, 161: 59–88.
- 1064 Voegelin, A.R., Nägler, T.F., Samankassou, E., Villa, I. M., 2009. Molybdenum isotopic  
1065 composition of modern and Carboniferous carbonates. *Chemical Geology* 265 (3–4), 488–  
1066 498.
- 1067 Waldron, J.W.F., Anderson, S.D., Cawood, P.A., Goodwin, L.B., Hall, J., Jamieson, R.A.,  
1068 Palmer, S.E., Stockmal, G.S., Williams, P.F., 1998. Evolution of the Appalachian Laurentian  
1069 margin: Lithoprobe results in western Newfoundland. *Can. J. Earth Sci.* 35: 1271–1287
- 1070 Waldron, J.W.F., Palmer, S.E., 2000. Lithostratigraphy and structure of the Humber Arm  
1071 Allochthon in the type area, Bay of Islands, Newfoundland. Newfoundland Department of  
1072 Mines and Energy, Geological Survey, Report 2000-1, 279–290.
- 1073 Wang, L., Azmy, K., 2020. Palaeoenvironmental changes in slope carbonates across the late  
1074 Cambrian–early Ordovician in western Newfoundland. *Geol. J.* 55 (5), 1–13.
- 1075 Wang, X., Liu, S-A., Wang, Z., Chen, D., Zhang, L., 2018. Zinc and strontium isotope  
1076 evidence for climate cooling and constraints on the Frasnian-Famennian (~372 Ma) mass  
1077 extinction. *Palaeogeography, Palaeoclimatology, Palaeoecology* 498, 68-82.
- 1078 Weber, T., John, S., Tagliabue, A., DeVries, T., 2018. Biological uptake and reversible  
1079 scavenging of zinc in the global ocean. *Science*, 361(6397), 72-76.
- 1080 Wei, H., Wang, X., Shi, X., Jiang, G., Tang, D., Wang, L. and An, Z., 2019. Iodine content of  
1081 the carbonates from the Doushantuo Formation and shallow ocean redox change on the  
1082 Ediacaran Yangtze Platform, South China. *Precambrian Research*, 322, pp.160-169.
- 1083 White, S.E., Waldron, J.W.F., 2018. Inversion of Taconian extensional structures during  
1084 Paleozoic orogenesis in western Newfoundland. In Wilson R.W., Houseman G.A.,  
1085 McCaffrey K.J.W., Doré A.G. and Buiter S.J.H. (eds) *Fifty Years of the Wilson Cycle*  
1086 *Concept in Plate Tectonics*. Geological Society, London, Special Publications, 470.

- 1087 White, S.E., Waldron, J.W.F., 2022. Along-strike variations in the deformed Laurentian  
1088 margin in the North Appalachians: Role of inherited margin geometry and colliding arches.  
1089 *Earth-Science Reviews* 226, 103931.
- 1090 Williams, H., 1978. Tectonic Lithofacies Map of the Appalachian Orogen, Map No. 1A;  
1091 International Geological Correlation Program, Project No. 27, The Appalachian-Caledonides  
1092 Orogen, Canadian Contribution No. 5.
- 1093 Williams, S.H., 1997. Graptolites, acritarchs and scolecodonts at Green Point, western  
1094 Newfoundland: International Cambrian-Ordovician Boundary Working Group, Circular  
1095 January 1997, 6-15.
- 1096 Williams, H., Hiscott, R.N., 1987. Definition of the Iapetus rift-drift transition in western  
1097 Newfoundland. *Geology*, v. 15, 1044–1047.
- 1098 Wignall, P.B., Twitchett, R.J., 1996. Ocean anoxia and the end-Permian mass extinction.  
1099 *Science* 272, 1155–1158.
- 1100 Wong, G.T.F., Brewer, P.G., 1977. Marine chemistry of iodine in anoxic basins: *Geochimica*  
1101 *et Cosmochimica Acta*, 41, 151–159.
- 1102 Wong, G.T.F., Piumsonboon, A. U., Dunstan, W.M., 2018. The transformation of iodate to  
1103 iodide in marine phytoplankton cultures. *Marine Ecology Progress Series*, vol. 237, 27-39,  
1104 2002.
- 1105 Wörndle, S., Crockford, P.W., Kunzmann, M., Bui, T.H. Halverson, G.P., 2019 Linking the  
1106 Bitter Springs carbon isotope anomaly and early Neoproterozoic oxygenation through  
1107 I/(Ca+Mg) ratios. *Chemical Geology* 524, 119-135.
- 1108 Yan, B., Zhu, X., He, X., Tang, S., 2019. Zn isotopic evolution in early Ediacaran ocean: a  
1109 global signature. *Precambrian Research* 320, 472–483.
- 1110 Young, S. A., Kleinberg, A., Owens, J. D., 2019. Geochemical evidence for expansion of  
1111 marine euxinia during an early Silurian (Llandovery-Wenlock boundary) mass extinction.  
1112 *Earth and Planetary Science Letters* 513, 187–196.
- 1113 Zhang, P., Wang, Y., Wei, Z., Wang, G., Zhang, T., He, W., Ma, X., Ma, H., Wei, J. and Zhu,  
1114 C., 2023. Influence of the Late Ordovician-Early Silurian Paleoenvironment and Related  
1115 Geological Processes on the Organic Matter Accumulation and Carbon Isotope  
1116 Excursion. *Paleoceanography and Paleoclimatology*, 38(7), p.e2023PA004628.
- 1117 Zhang, S., Barnes, C.R., 2004. Late Cambrian and Early Ordovician conodont communities  
1118 from platform and slope facies, western Newfoundland: a statistical approach. *Geological*  
1119 *Society, London, Special Publications*, 230, 47–72.
- 1120 Zhang, T., Sun, R. Liu, Y., Chen, L., Zheng, W., Liu, C-Q., Chen, J., 2022. Copper and Zinc  
1121 isotope signatures in scleractinian corals: Implications for Cu and Zn cycling in modern and  
1122 ancient ocean. *Geochimica et Cosmochimica Acta*, 317, 395-408.
- 1123 Zhao, M., Tarhan, L.G., Zhang, Y., Hood, A., Asael, D., Reid, R.P, Planavsky, N.J., 2021.  
1124 Evaluation of shallow-water carbonates as a seawater zinc isotope archive. *Earth and*  
1125 *Planetary Science Letters* 553, 116599.
- 1126 Zhao, Y., Vance, D., Abouchami, W., De Baar, H.J.W., 2014. Biogeochemical cycling of  
1127 zinc and its isotopes in the Southern Ocean: *Geochimica et Cosmochimica Acta*, v. 125, 653–  
1128 672, doi:10.1016/j.gca.2013.07.045.

- 1129 Zhao, Z., Ahlberg, P., Thibault, N., Dahl, T.W., Schovsbo, N.H., Nielsen, A. T., 2022. High-  
1130 resolution carbon isotope chemistratigraphy of the middle Cambrian to lowermost Ordovician  
1131 in southern Scandinavia: Implications for global correlation. *Global and Planetary Change*, v.  
1132 209, 103751.
- 1133 Zhou, X., Jenkyns, H.C., Owens, J.D., Junium, C.K., Zheng, X-Y., Sageman, B.B., Hardisty,  
1134 D.S., Lyons, T.W., Ridgwell, A., Lu, Z. 2015. Upper ocean oxygenation dynamics from I/Ca  
1135 ratios during the Cenomanian-Turonian OAE 2. *Paleoceanography*, 30, 510–526.
- 1136 Zhou, L., Algeo, T.J., Shen, J., Hu, Z., Gong, H., Xie, S., Huang, J., Gao, S., 2015. Changes  
1137 in marine productivity and redox conditions during the Late Ordovician Hirnantian  
1138 glaciation. *Palaeogeography, Palaeoclimatology, Palaeoecology*, 420, 223–234.

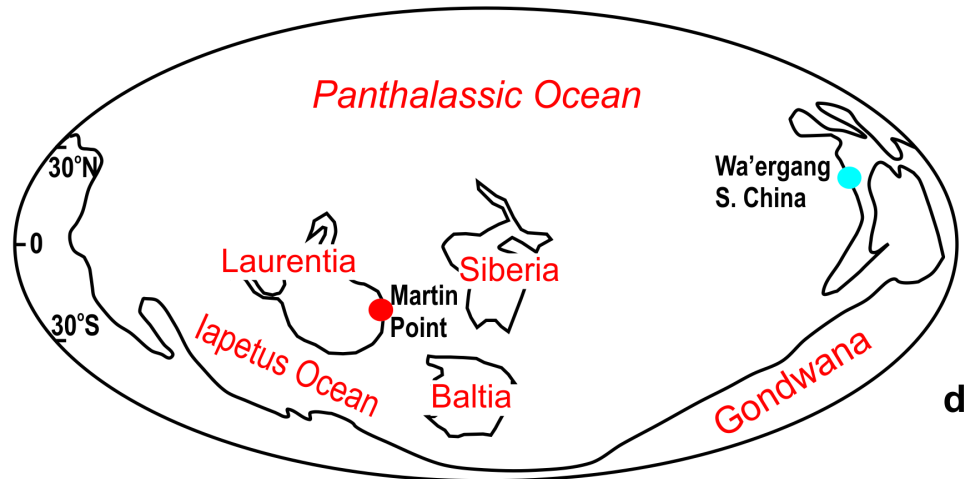
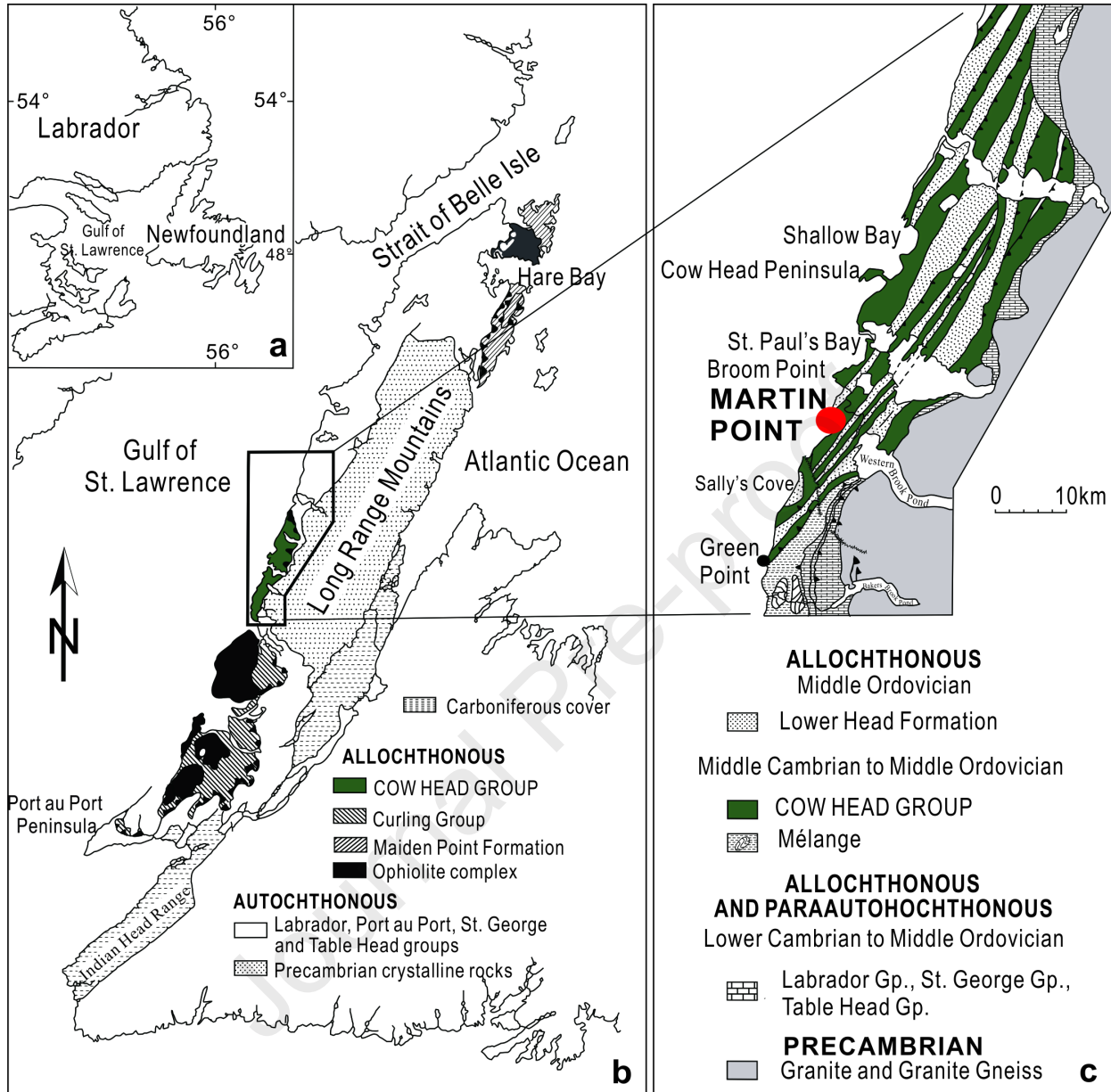


## Post-SPICE (NL 1 and NL 2)

B1-3	-1.68	0.43	+0.37		309259	9029	6.5	186	238	7.0	6.2	536	9363	4704	15.2	0.34	97	1.41	2.45	20.5	33.0	3.9	13.5	2.1	0.51	2.2	0.29	1.5	0.30	0.79	0.11	0.71	0.10	
B2-1	-3.85		+0.24		343808	9844	16.5	187	512	8.4	5.7	462	12750	4275	12.3	1.05	87	1.32	0.64	29.7	45.1	5.4	18.3	2.7	0.66	2.9	0.39	2.0	0.38	0.95	0.12	0.74	0.10	
B2-2	-2.28		+0.34		332864	15595	5.8	203	132	7.0	2.6	584	10495	5114	17.6	0.29	106	1.12	0.98	23.1	37.3	4.5	15.3	2.4	0.62	2.5	0.38	2.1	0.43	1.16	0.16	1.00	0.14	
B4-1	-2.40	0.24	+0.14	0.04	381857	2695	4.0	200	103	1.0	0.6	169	1169	1159	4.2	0.04	36	0.27	0.11	4.4	7.7	0.8	2.9	0.4	0.08	0.4	0.05	0.2	0.05	0.12	0.02	0.11	0.02	
B6	-1.30	0.20	+0.21	0.40	246336	11351	6.6	172	232	4.4	4.4	225	6748	3202	8.7	0.15	138	1.55	0.35	15.0	27.6	3.4	12.0	1.9	0.39	1.9	0.24	1.1	0.20	0.52	0.07	0.46	0.07	
B10	-0.58	0.10	+0.33	0.14	304114	4197	2.8	158	147	2.4	1.6	222	3532	2037	5.2	0.13	31	1.26	0.94	10.4	20.6	2.2	8.2	1.3	0.31	1.5	0.20	1.0	0.20	0.55	0.08	0.53	0.08	
B12	-1.38	0.28																																
B14-1	-0.96		+0.28	0.18	307080	7481	7.5	123	241	8.9	4.1	210	5631	4581	15.7	0.48	88	2.19	1.80	10.1	19.0	2.1	7.5	1.2	0.27	1.2	0.15	0.7	0.14	0.37	0.05	0.35	0.05	
B14-2	-0.02	0.34	+0.37		338646	3734	2.5	285	138	2.2	1.4	182	2147	1499	5.2	0.11	41	0.80	0.46	15.8	27.9	3.4	11.5	1.7	0.39	1.7	0.22	1.0	0.19	0.49	0.07	0.44	0.06	
B14-3	-0.67	0.30	+0.31	0.04	296687	6945	7.1	308	125	7.6	4.2	196	7534	5365	16.8	0.11	170	1.90	0.36	11.8	23.7	2.6	9.1	1.4	0.32	1.4	0.18	0.9	0.17	0.43	0.06	0.39	0.06	
B16-1	-0.41																																	
B16-3	-0.32	0.18		0.08	265878	7243	7.4	161	265	8.3	5.0	395	7687	7746	27.1	0.20	137	2.11	2.21	23.2	46.0	4.7	17.2	2.8	0.65	2.8	0.38	2.0	0.39	1.03	0.15	0.95	0.14	
B18-1	-0.74																																	
B18-2			+0.19		330487	2230	2.2	182	220	2.0	1.4	317	2035	1567	5.6	0.12	36	0.79	0.93	25.6	44.7	4.8	16.7	2.5	0.60	2.8	0.38	2.1	0.44	1.25	0.19	1.27	0.19	
B19	-0.76	0.17																																
B20-2	-0.48																																	
B22-1	-0.42	0.20	+0.26	0.15	351568	2964	2.1	268	40	3.0	1.8	180	2228	1038	1.9	0.05	20	0.41	0.18	5.6	10.2	1.1	3.8	0.6	0.13	0.7	0.08	0.4	0.08	0.20	0.03	0.19	0.03	
B22-3	-1.06																																	
B22-5	-1.51	0.18	+0.38		309473	11763	2.9	150	123	2.3	2.0	273	6422	2374	8.0	0.37	26	0.98	1.29	14.0	24.9	2.8	10.0	1.6	0.37	1.9	0.24	1.2	0.24	0.65	0.09	0.63	0.09	
B23-2	-0.94	1.46																																
B23-3	-1.31																																	
B23-6	-1.32		+0.41	0.38	338553	8883	3.0	190	108	2.7	2.1	189	6206	1366	4.2	0.44	38	0.90	0.69	21.9	34.4	4.1	14.1	2.1	0.47	2.4	0.30	1.4	0.28	0.73	0.11	0.70	0.10	
B23-9	-0.39	1.25	+0.34	0.17	389269	2188	1.9	973	56	1.5	1.4	132	2106	447	4.5	0.12	19	0.28	1.25	5.1	8.7	0.8	2.9	0.4	0.10	0.5	0.06	0.3	0.06	0.17	0.02	0.14	0.02	
B27-1	-0.59																																	
B29-3	+0.30	1.76	+0.25	0.388	308687	6788	6.6	408	152	10.8	6.7	99	10904	2366	24.0	0.91	84	1.83	0.76	12.3	23.5	2.7	10.0	1.7	0.38	1.7	0.24	1.3	0.25	0.65	0.09	0.59	0.09	
B29-5	-0.07																																	
B29-7	-0.79	0.56																																
B31-2	-0.11		+0.36		341107	10279	3.9	182	72	2.4	1.5	157	6120	1372	5.7	0.36	39	1.14	0.58	13.7	25.3	2.8	10.2	1.7	0.39	1.9	0.25	1.2	0.23	0.61	0.09	0.56	0.08	
B31-3	+0.27																																	
B31-4	+0.70	1.09	+0.23	0.25	391818	6066	7.8	236	130	3.4	3.2	189	4769	2258	5.1	0.39	50	1.16	1.25	10.1	21.5	2.3	8.5	1.4	0.34	1.7	0.23	1.1	0.23	0.60	0.09	0.54	0.08	
B31-7																																		
B31-9	+0.68	0.94	+0.34		387574	5049	4.0	284	114	0.9	0.8	160	2002	459	1.7	0.40	16	0.41	0.32	21.2	32.0	4.1	13.8	2.1	0.51	2.4	0.32	1.5	0.29	0.74	0.10	0.65	0.09	
B31-11	-0.38																																	
B32	-0.69	0.50	+0.73	0.04	221926	127353	3.6	121	249	3.2	4.7	489	22474	2669	11.9	0.36	26	1.42	0.68	11.0	20.5	2.3	8.8	1.5	0.36	1.7	0.24	1.1	0.23	0.59	0.08	0.52	0.07	
B33-2	+0.96	1.52																																
B35-1	-0.88		+0.58		431121	4698	0.8	241	124	0.8	0.5	163	1533	721	2.4	0.10	13	0.47	1.27	10.2	17.4	2.0	7.5	1.2	0.29	1.4	0.19	0.9	0.18	0.47	0.06	0.40	0.06	
B35-3	-1.40	2.98	+0.34	0.32	335460	5112	1.2	358	150	12.2	7.0	201	14175	1253	4.9	3.41	30	0.85	1.013	15.1	30.2	3.6	13.1	2.3	0.53	2.2	0.33	1.7	0.33	0.84	0.12	0.77	0.11	
B36a-2	-4.79	0.52	+0.26	0.31	363958	6461	12.1	204	166	3.7	2.0	906	5277	3603	6.0	0.07	30	1.25	0.27	12.0	22.6	2.7	9.8	1.5	0.37	1.9	0.24	1.2	0.24	0.62	0.09	0.55	0.08	
B36a-3	-0.80	0.51	+0.19	0.10	270053	5092	20.7	228	332	24.8	13.7	672	38862	4957	14.4	3.32	91	1.65	1.62	21.3	44.9	5.4	20.6	3.7	0.89	3.7	0.55	2.9	0.57	1.46	0.20	1.25	0.18	
B36a-4	-1.29	0.53	+0.37		327222	7489	9.3	275	365	11.6	8.3	848	27412	4527	8.5	0.86	42	1.80	1.65	20.5	42.8	5.2	20.6	3.7	0.92	4.2	0.59	3.0	0.59	1.49	0.20	1.27	0.18	
B36a-5	-3.92	0.78																																
B36a-6	-2.66		+0.44	0.31	350454	5014	4.0	198	160	5.6	3.2	1051	6882	5716	9.0	0.17	39	1.69	0.69	14.8	29.4	3.6	13.4	2.2	0.52	2.5	0.34	1.7	0.33	0.87	0.12	0.76	0.11	
B36c-1	-0.12		+0.12		393491	8794	41.5	453	231	3.8	2.1	302	7627	3070	6.0	0.42	29	1.12	0.77	18.1	32.4	3.9	14.4	2.4	0.57	2.7	0.36	1.7	0.31	0.77	0.10	0.64	0.09	
B36c-2	+0.56																																	
B36c-3	+0.32		+0.35	0.28	415615	6989	4.8	705	151	4.3	1.7	267	6316	4161	6.4	0.27	55	1.29	0.49	10.8	21.3	2.7	10.2	1.7	0.42	1.8	0.25	1.2	0.23	0.59	0.08	0.51	0.07	
B36c-4	-1.96	0.44	+0.33	0.56	417751	9697	4.5	587	327	3.5	3.2	199	6032	4794	8.9	0.61	54	1.13	0.56	15.7	31.6	4.1	15.9	2.7	0.64	2.9	0.40	1.8	0.34	0.83	0.11	0.69	0.10	
B36d-1	-0.72																																	
B36d-2	-1.04	0.80	+0.46	0.26	466606	6170	2.11	470	139	3.0	5.8	303	4648	5721	11.3	0.09	48	0.73	0.66	9.6	18.4	2.1	7.8	1.3	0.32	1.5	0.21	1.1	0.23	0.65	0.10	0.63	0.10	

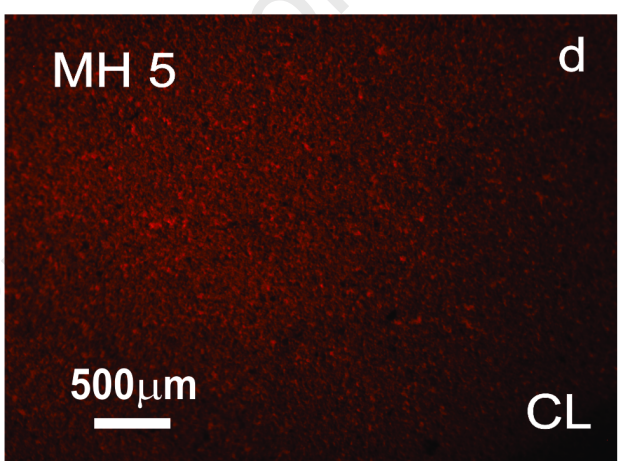
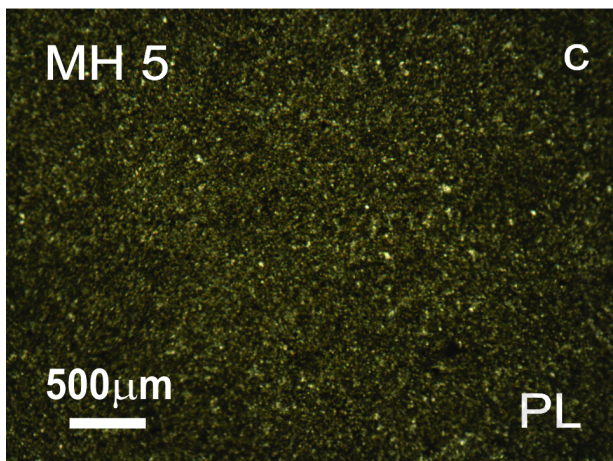
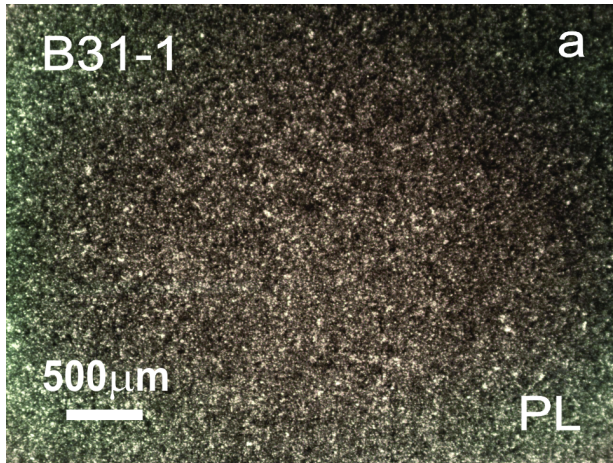
	$\delta^{13}\text{C}_{\text{carb}}$ (‰ VPDB)	TOC (%)	$\delta^{66}\text{Zn}$ (‰ JMC Lyon)	I/(Ca+Mg) $\mu\text{mol/mol}$	Zn (ppm)	Sr (ppm)	P (ppm)	Ni (ppm)	Cu (ppm)	Mn (ppm)	Fe (ppm)	Al (ppm)	$\Sigma\text{REE}$ (ppm)	V (ppm)	Mo (ppm)	Th/U	Mn/Al	Fe/Al	Al/Ti
<b>HERB</b>																			
<i>n</i>	48	36	18	11	11	17	17	17	17	17	17	17	17	17	17	17	17	17	17
Mean	-0.6	1.02	0.33	0.13	6.2	356	142	4.1	7.6	380	2542	1436	49	4.9	2.5	1.4	0.35	1.7	38.4
STDV	0.8	0.62	0.11	0.09	7.6	226	45	1.9	3.1	142	1876	791	22	1.5	2.6	1.5	0.25	0.8	13.8
MAX	1.0	3.10	0.48	0.31	21.7	980	252	8.5	17	572	6900	3202	95	7.8	11.7	5.1	0.93	4.5	79.6
MIN	-2.1	0.30	0.09	0.02	0.6	165	85	1.9	4.7	150	785	611	25	2.2	0.8	0.1	0.11	1.1	19.3
<b>post-SPICE (NL1 &amp; NL2)</b>																			
<i>n</i>	46	26	29	19	30	30	30	30	30	30	30	30	30	30	30	30	30	30	30
Mean	-0.94	0.70	0.33	0.18	6.9	290	185	5.4	3.6	343	8370	3137	65	9.3	0.53	1.8	0.13	3.1	61.3
STDV	1.18	0.66	0.13	0.13	7.9	188	102	4.9	2.8	247	8196	1907	26	6.3	0.81	1.2	0.08	2.5	33.2
MAX	0.96	2.98	0.73	0.48	41.5	973	512	24.8	13.7	1051	38862	7746	109	27.1	3.41	5.3	0.35	11.3	146.2
MIN	-4.79	0.10	0.12	0.02	0.8	121	40	0.8	0.5	99	1169	447	17	1.7	0.04	0.2	0.04	0.8	23.2

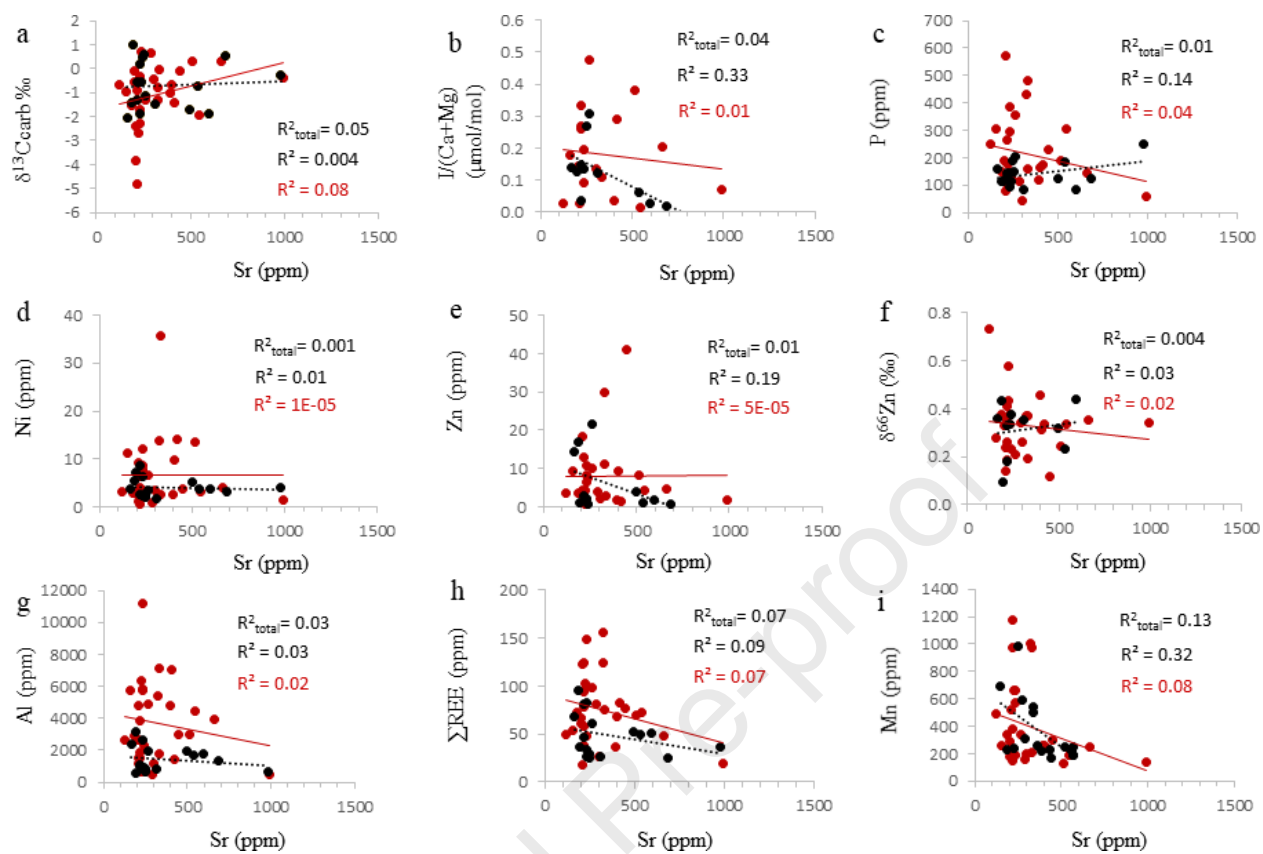
Journal Pre-proof

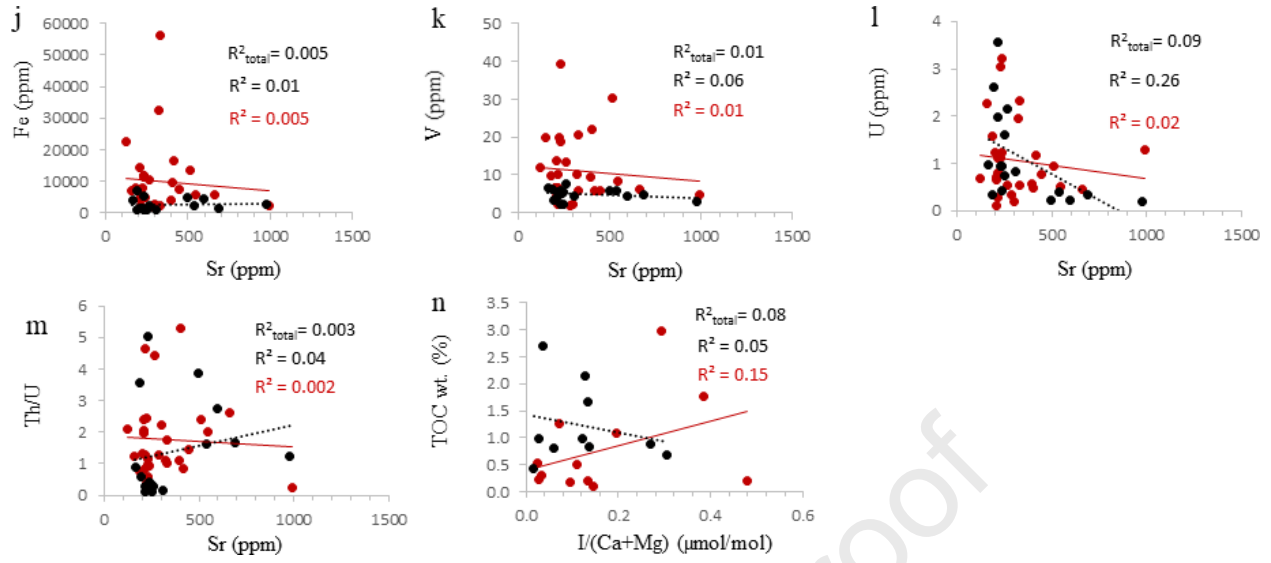


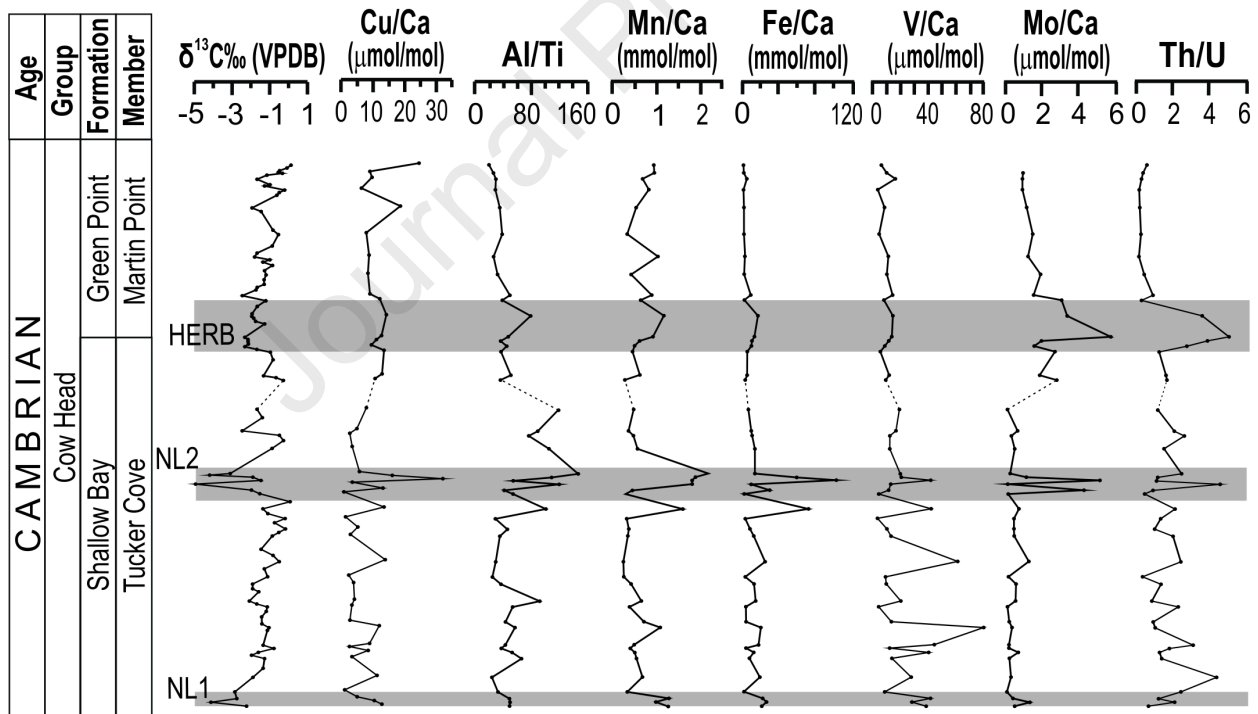
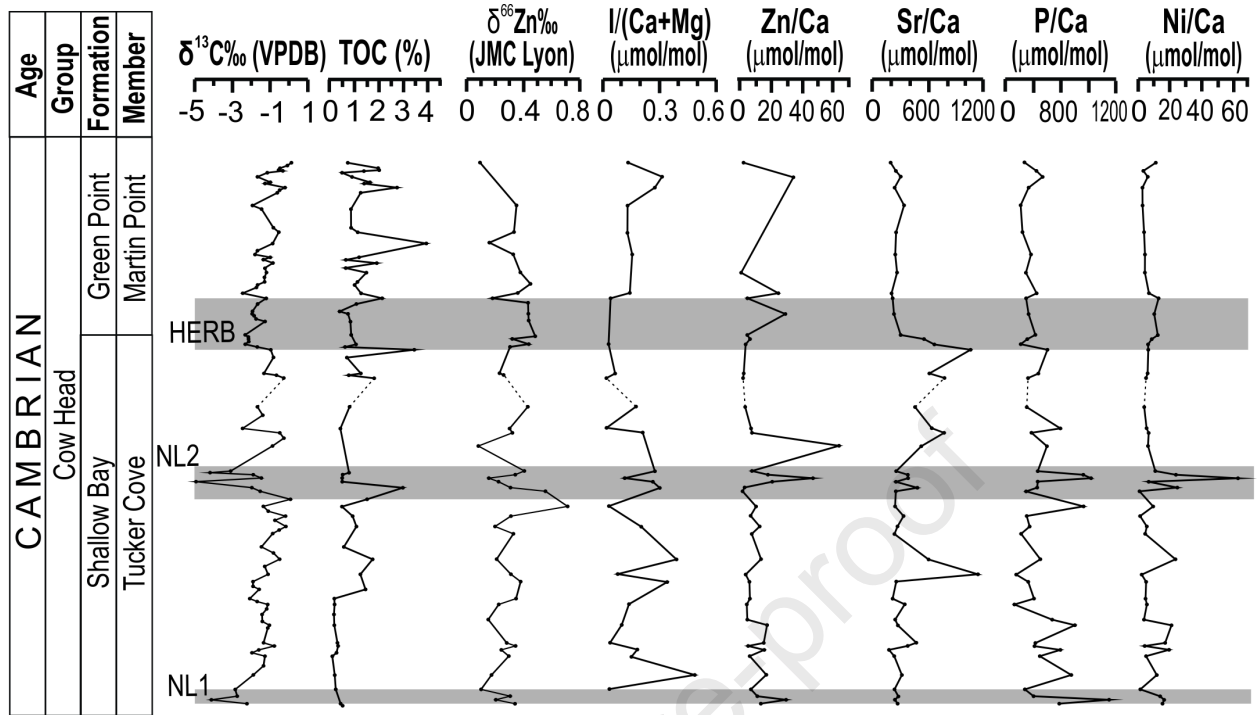
Journal Pre-proof











## Highlights

- Upper Cambrian carbonates in western Newfoundland retaining at least near-primary paleoenvironmental proxy signatures.
- Organic-rich water shoaling into a shallow environment and leading to dysoxic conditions.
- Zn isotope and  $I/(Ca+Mg)$  ratios consistent with abundant low-oxygen conditions.

Journal Pre-proof

### **Declaration of competing interest**

The authors declare that they have no known competing financial interests or personal relationships that could have appeared to influence the work reported in this paper.

Journal Pre-proof